Spontaneous Formation of an Internal Shear Band in Ice Flowing over Topographically Variable Bedrocks

Emma Weijia Liu[1], Ludovic Räss[2,3], Frédéric Herman[4], Yury Podladchikov[5], Jenny Suckale[1]

[1]Geophysics Department, Stanford University, USA
[2]Laboratory of Hydraulics, Hydrology and Glaciology (VAW), ETH Zurich, Switzerland
[3]Swiss Federal Institute for Forest, Snow and Landscape Research (WSL), Switzerland
[4]Institute of Earth Surface Dynamics, University of Lausanne, Switzerland
[5]Institute of Earth Sciences, University of Lausanne, Switzerland

Key Points:

- Ice flowing over rough basal topography may spontaneously develop an internal shear band on topographic highs.
- Two competing mechanisms control the energy balance near the bedrock: vertical advective cooling and internal shear heating.
- We summarize how basal topography and the rheological power-law exponent influence shear band formation in a regime diagram.

Corresponding author: Emma Weijia Liu, liuwj@stanford.edu

Abstract

Ice surface speed increases dramatically from upstream to downstream in many ice streams and glaciers. This speed-up is thought to be associated with a transition from internal, distributed deformation to highly localized deformation at the ice-bedrock interface. The physical processes governing this transition remain unclear. Here, we argue that basal topography can give rise to internal shear localization. The power-law rheology exponent n amplifies the feedback between shear heating and localization, leading to the spontaneous formation of an internal shear band that creates flow separation within the ice. We model the thermo-mechanical ice flow over a sinusoidal basal topography by building on the high-resolution Stokes solver FastICE v1.0. To capture the interactions between ice and rock, we implement an Immersed Boundary Method and use a level-set approach to represent the free surface of the ice. We compile a regime diagram summarizing when a sinusoidal topography with a given amplitude and wavelength lead to shear band formation for a given rheology. We compare our model results to borehole measurements from Greenland and find evidence that supports the existence of a shear band.

Plain Language Summary

On its way towards the ocean, ice speeds up dramatically from less than one meter per year inland to more than a kilometer per year downstream. In this paper, we investigate the physical processes controlling this speed-up. More specifically, we focus on the role that the bedrock topography underneath the ice and the rheology might play to facilitate this transition. We use a two-dimensional numerical model to simulate the flow field within a slab of ice flowing down a ramp over a simplified topography. We find that including basal topography can lead to a zone of highly localized deformation within the ice above topographic highs. We compare our model results to borehole measurements from Greenland and find evidence that supports the existence of a shear band.

1 Introduction

The world's two largest ice sheets, Antarctica and Greenland, discharge most of their ice mass through fast-moving ice stream and mountain glaciers (Joughin et al., 2010; Rignot et al., 2011). On its path toward the ocean, ice initially moves at relatively low speeds of about one meter per year (Rignot et al., 2011), but then speeds up dramatically reaching surface speeds more than a kilometer per year in some ice stream and glaciers (Rignot et al., 2002; Joughin et al., 2003; Mouginot et al., 2014). The speed-up is thought to be associated with a transition from flow through internal, distributed deformation to sliding, accommodated by highly localized deformation at the ice-bedrock interface (Clarke, 1987; Whillans et al., 1987). This transition from slow flow inland to rapid sliding in outlets is known as the flow-to-sliding transition.

One potential explanation for the flow-to-sliding transition is thawing of the bed, since ice moving over a temperate bed can slide while ice frozen onto the bed must deform internally. The creep instability could facilitate thawing (Robin, 1955) because deformation is most pronounced in cold ice near the bed, leading to shear weakening and intensified deformation until temperature reaches the pressure melting point (Clarke et al., 1977; Yuen & Schubert, 1979). However, it remains unclear how viable this explanation is, as first mentioned in Nye (1971) and later substantiated by Larson (1980) and Fowler (2001) who showed that the local conservation of flux implies a reduction in shearing, translating into less energy release and refreezing. Bueler (2009) identified the advection of cold ice to the warm bed as the main impediment for a sudden transition to sliding; an argument further developed by Mantelli et al. (2019).

The work by Bueler (2009) and Mantelli et al. (2019) suggests that the flow-to-sliding transition does not happen suddenly, but gradually over an extended distance in the flow

direction. What are the physical processes governing this transition and the scale over which it occurs? Clues come from borehole measurements (Lüthi et al., 2002; Ryser et al., 2014; Harrington et al., 2015; Hills et al., 2017; Doyle et al., 2018; Maier et al., 2019; Law et al., 2023) suggest a complex, depth-dependent velocity field in the ice above a topographicly variable bed. Many factors may contribute to this variability, including the presence of sediments and sediment-freeze-on (Herron et al., 1979; Gow et al., 1979; Goodwin, 1993; Carsey et al., 2002), subglacial hydrology (Doyle et al., 2018), seasonal cycles (Ryser et al., 2014), paleo history (Lüthi et al., 2002), and variable topography (Law et al., 2023). Here, we focus specifically on the role of variable topography as a first step towards a more complete understanding.

The goal of this paper is to understand the impact of topographically uneven hard bedrock on ice flow acceleration by quantifying shear localization in the vicinity of the bedrock using numerical simulations. Several prior studies have investigated the role of topography on the thermo-mechanical deformation of sliding ice (e.g., Gudmundsson, 1997; Helanow et al., 2020, 2021). Our work complements these existing contributions by focusing on flowing ice, prior to the onset of sliding. We hypothesize that the intense deformation of cold ice flowing over sufficiently pronounced basal topography can lead to the formation of an internal shear band connecting topographic highs that accounts for most of the internal deformation within the ice. Similarly to flow separation in sliding ice (Gudmundsson, 1997), we expect that the conditions for shear band formation depend on both the topography imposed and the rheology imposed, most notably the degree of non-linearity embedded into the rheology through the power-law exponent n.

We test our hypothesis through numerical simulations, building on recent advances in simulating the thermo-mechanical deformation of ice at high resolution implemented in FastICE v1.0 (Räss et al., 2020). We add to the original release of FastICE v1.0 by incorporating a free surface and variable basal topography since both are critical for the physical process that we aim to understand. We capture the free ice surface using a level-set representation (Osher & Sethian, 1988; Sethian & Smereka, 2003) and the basal topography through an Immersed-Boundary Method (Peskin, 1972, 2002). The deformation of ice depends sensitively on ice rheology, because different rheology formulations can imply orders of magnitude differences in the response of ice deformation to stresses. To gain insights into the influence of rheology on shear band formation, specifically the rheological power-law exponent n, we also consider different values of exponent from $n = 1$ to $n = 4$.

Recently, Law et al. (2023) provides compelling evidence for complex, depth-dependent ice motion for three glaciers in Greenland, Sermeq Kujalleq/Store Glacier and Isunnguata Sermia Glacier, consistent with the idea of flow separation by Gudmundsson (1997). By linking field observations and numerical simulations, Law et al. (2023) show that both the vertical extent of temperate ice near the bed and the portion of deformation accommodated by basal slip varies significantly at the field-site scale and call for an improved parametrization of this variability in ice-sheet models. They also show that mostly used bedrock topography such as BedMachine (Morlighem et al., 2017) is too coarse and smooth. Thus using geostatistically more accurate realisation of bedrock topography results in rougher bedrock and enhanced shear localization. Deriving an improved parameterization requires an improved understanding of the physical processes governing the observed complexities in depth-dependent ice motion. We intentionally focus on an idealized sinusoidal topography to advance this process-based understanding. We synthesize our simulation results into a regime diagram that summarizes how the formation of an internal shear band depends on both the amplitude and wavelength of the underlying topography and on the assumed ice rheology.

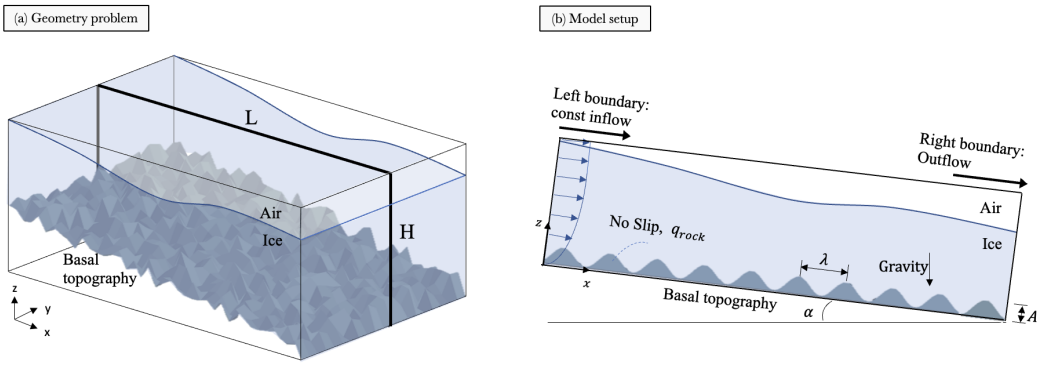

Figure 1. Model geometry of ice sheet flowing over rough hard bedrock. (a) The general case of a slab of ice flowing over rough hard bedrock in three-dimensions with a free surface. (b) The two-dimensonal model setup with a sinusoidal basal topography and a free surface.

2 Methods

To approximate the thermo-mechanical deformation within a slab of ice flowing over a rough hard bedrock in the downstream direction x (Figure 1, a), we neglect variability in the transverse direction y. This choice reduces our modeling domain to a two-dimensional, along-flow cut through the three-dimensional ice slab along the thick black line (Figure 1, a). The depth direction z is oriented vertically upwards from the bedrock. The origin of the axes $(x = 0, z = 0)$ locates at the bedrock of the flow inlet. The size of the model domain is $(0, L) \times (0, H)$, and it is tilted at an angle α. To represent basal topography, we adopt an idealized sinusoidal contour $z = A \sin(kx)$ with an amplitude A and a wavenumber k. We include a thin layer of low-viscosity phase on top of the ice to mimic the presence of air, which allows ice thickness to change spatially and temporally.

We capture the depth-dependent thermo-mechanical ice deformation implementing an incompressible viscous Stokes solver using the time-dependent implicit pseudo-transient methods and the finite difference discretization (Räss et al., 2020; Räss et al., 2022). To prescribe the basal ice-bedrock boundary condition, we implement the Immersed Boundary Method, a fictitious domain method that allows to treat fluid and structural domains separately (Peskin, 1972, 2002). To incorporate the free surface boundary condition, we use the level-set Methods, an implicit description for moving fronts further advected with the local fluid velocity (Sethian & Smereka, 2003; Osher et al., 2004). The implementations of ice-bedrock and ice-air boundary condition are discussed in Section 2.2.

2.1 Thermo-mechanical Model

We describe ice as an incompressible, non-linear, viscous fluid with a temperature-dependent rheology. The momentum equations are

$$\frac{\partial \tau_{ij}}{\partial x_j} - \frac{\partial p}{\partial x_i} + F_i = 0, \qquad \tau_{ij} = 2\eta \dot{\epsilon}_{ij}\,, \tag{1}$$

where $F_i = \rho g(\sin\alpha, \cos\alpha)$ is the gravitational body force at a tilted angle α, p is isotropic pressure, τ_{ij} is the deviatoric stress tensor, $\dot{\epsilon}_{ij}$ is the shear strain rate tensor, and η is the ice viscosity. Reducing the model to two dimensions implies that all components in the transverse direction y are zero. The only non-zero shear strain rate and shear stress are $\dot{\epsilon}_{zx}$ and τ_{zx}, respectively.

Ice flows into the domain from the left boundary over an undeforming hard bedrock, and exits at the right boundary. We calculate the analytical inflow field by solving the momentum balance along the flow at steady state

$$\eta(z)\frac{\partial u}{\partial z} = \rho g(H-z)\sin\alpha, \quad \eta(z) = \eta_b + (\eta_s - \eta_b)\frac{z}{H}, \tag{2}$$

where we assume a linear viscosity profile between the viscosity at the bed, η_b, and the viscosity at the surface, η_s. Integrating equation (2), we have the analytical inflow velocity

$$u_{\text{inlet}} = \frac{\rho g \sin\alpha}{K^2}\left[\eta_b \log\left(\eta_b + Kz\right) + KH\log\left(\eta_b + Kz\right) - Kz\right] + C, \tag{3}$$

where $K = (\eta_s - \eta_b)/H$, and C is the integration constant such that the velocity at bed is zero. When viscosity is constant throughout the domain, $\eta_s = \eta_b = \eta_0$, the analytical inflow velocity simplifies to a parabolic velocity profile $u_{\text{inlet}} = \rho \sin\alpha/\eta_0(Hz - 0.5z^2)$.

At the outlet, we adapt the outflow boundary condition from Orlanski (1976)

$$\frac{\partial u}{\partial t} + U\frac{\partial u}{\partial x} = 0, \tag{4}$$

where U is the propagation velocity. Following the approach by Kreiss (1968), we estimate it numerically by calculating the propagation velocity between neighboring grid points $U = \Delta x/\Delta t$, where Δx and Δt are the spatial and temporal grid sizes, respectively. The extrapolated velocity at the outlet boundary is then

$$u_{n_x}^{n_t} = 2u_{n_x-1}^{n_{t-1}} - u_{n_x-2}^{n_{t-2}}, \tag{5}$$

where n_x is the boundary point and n_t is the current time step.

At the ice surface, we assume that the atmospheric pressure is negligible relative to the pressure in the ice column, implying a stress-free surface

$$\sigma_{ij} n_j = 0. \tag{6}$$

where n_j is the normal vector to the ice surface, σ_{ij} is the Cauchy stress tensor, obtained by combining the isotropic pressure p and the deviatoric stress τ_{ij}. In addition, we impose a constant atmospheric temperature at ice surface $T_{\text{s}} = -26^{\text{o}}\text{C}$.

At the ice-bedrock interface, we assume ice is frozen to bed and impose a no-slip boundary condition. We implement this boundary condition using the Immersed Boundary Methods. In addition, we impose a constant geothermal heat flux of 0.05W/m^2 (Wright et al., 2012; Shapiro & Ritzwoller, 2004; Maule et al., 2005). The details are discussed in Section 2.2.

The thermal model takes into account the effects of diffusion, advection, shear heating, and melt water weakening. We curtail the temperature at $T_m = -0.1$ °C and estimate the melt rate with the latent heat. The energy equation is given by

$$\rho c_p\left(\frac{\partial T}{\partial t} + u_i\frac{\partial T}{\partial x_i}\right) = \frac{\partial}{\partial x_i}\left(\kappa\frac{\partial T}{\partial x_i}\right) + 2\tau_E\dot{\epsilon}_E - L\dot{m}, \tag{7}$$

where c_p is the specific heat of ice, κ is the thermal conductivity, τ_E and $\dot{\epsilon}_E$ are effective shear stress and effective shear strain rate, respectively. The term $2\tau_E\dot{\epsilon}_E$ represents shear heating, $L\dot{m}$ captures the energy required for melting where $L = 0.366\times10^6\text{J/kg}$ is the latent heat, and $\dot{m}$ is the generated melt water flux.

In the temperate zone where temperature is around the melting point, as defined by the logistic function

$$f(T - T_m) = 1 - \tanh\left(-0.5(T - T_m)\right), \tag{8}$$

we assume that the shear heating $2\tau_E\dot{\epsilon}_E$ is absorbed for the phase change from ice to water (Suckale et al., 2014; Räss et al., 2020). The temperature in the temperate zone can hence not exceed the pressure melting point, leading to the simplified energy equation

$$\rho c_p \left(\frac{\partial T}{\partial t} + u_i \frac{\partial T}{\partial x_i} \right) = \frac{\partial}{\partial x_i} \left(\kappa \frac{\partial T}{\partial x_i} \right) + 2\tau_E \dot{\epsilon}_E f(T - T_m). \tag{9}$$

The logistic function (8) serves as an indicator of how close the ice temperature is to the melting point T_m. When the temperature has reached the melting point, i.e., $f(T-T_m) = 0$, all shear heating is absorbed to for the phase change from ice to water, and no net heat source is added to energy equation.

The time dependence of the problem comes from the free surface evolution and from the energy equation because the shear heating, diffusion and advection terms are transient. At each physical time step, we use the pseudo-transient method (Räss et al., 2022) to solve the system of coupled momentum equation (1) and energy equation (9) iteratively until the continuity residual, $\partial p/\partial \tau_p$, momentum residual, $\partial u_i/\partial \tau_u$, and temperature residual, $\partial T/\partial \tau_T$, are minimized, achieving an implicit solution of the equations. Thus, the governing equations in a residual form are

$$\frac{\partial p}{\partial \tau_p} = -\frac{\partial u_i}{\partial x_i}, \tag{10}$$

$$\frac{\partial u_i}{\partial \tau_u} = \frac{\partial \tau_{ij}}{\partial x_j} - \frac{\partial p}{\partial x_i} + F_i, \tag{11}$$

$$\frac{\partial T}{\partial \tau_T} = -\frac{\partial T}{\partial t} - u_i \frac{\partial T}{\partial x_i} + \frac{1}{\rho c_p} \left(\frac{\partial}{\partial x_i} \left(\kappa \frac{\partial T}{\partial x_i} \right) + 2\tau_E \dot{\epsilon}_E f(T - T_m) \right), \tag{12}$$

where τ presents the pseudo time step, and t represents physical time step.

The key limiting factor of the convergence rates of equations (10) to (12) is the convergence rate of the ice viscosity. During iterations in pseudo time, we do not evolve the ice surface. After the residuals fall below the defined thresholds indicating that the numerical solution has reached steady state, we advect the free surface with the local ice velocity. The details of the advection of the free surface is presented in Section 2.2.

We adopt a power-law relationship for the rheology model and specifically investigate the power-law with different values of the exponent n

$$\dot{\epsilon}_{ij} = a \tau_{II}^{n-1} \exp\left(-\frac{Q}{R(T_s + T)} \right) \tau_{ij} \ , \tag{13}$$

where a is pre-factor, Q the activation energy, R the universal gas constant, and T_s the surface temperature.

One challenge in implementing the power-law rheology is that the pre- factor a is difficult to constrain experimentally or observationally, partly because it captures several different physical processes, such as grain size, temperature, fabrics, and other variables (Paterson, 1994).

In our model, a depends only on temperature and interstitial water content, and we neglect other dependencies mostly because limited data exists to constrain these. The temperature dependency is described as Arrhenius relationship in equation (13). To capture the viscosity-weakening effect of interstitial water, we define an additional parameter a_w. In our model, we use the same logistic function from equation (8) that reads $a_w = (1-f(T-T_m))$ in the energy equation to capture viscous weakening in the presence of water for the power-law (Suckale et al., 2014). Thus, our implementation of the pre-factor is $a = a_0 a_w$, where a_0 is treated as constant and comes from other dependencies such as grain size and fabrics.

It is important to note that interstitial water can impact not only the pre-factor a, but also the exponent n. Recent research by Adams et al. (2021) suggests that the

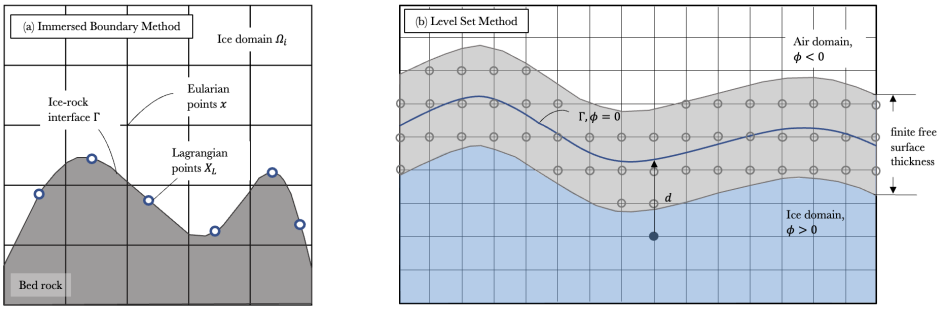

Figure 2. Illustration of Immersed Boundary Method and level-set Method. (a): Treatment of the ice-bedrock interface. The spatial discretization of the ice domain, Ω_i, and bed shape, Γ. Ω_i is discretized in a Cartesian grid x. The ice-bedrock interface, Γ, is discretized using Lagrangian points X_l. (b): Treatment of the ice-air interface. The domain is divided into ice (blue) and air (white) domains using a level-set function with a finite but very small free surface thickness (light grey) of $3\Delta x$.

exponent for temperate ice with sufficient interstitial water is close to 1.1. Other studies have also found similar enhancements in creep rates as ice approaches pressure melting point (e.g., Mellor & Testa, 1969; Barnes, Tabor, & Walker, 1971). However, due to limited data to accurately constrain the effect of interstitial water on the value of n, our model does not consider this impact.

2.2 Implementation of the Basal Interface and Free Surface

To simulate the mechanical and thermal interactions along the ice-bedrock interface Γ, we integrate the Immersed Boundary Method (IBM) (Peskin, 1972, 2002) into the Stokes solver. IBM is a fictitious domain method that discretizes the ice and rock phases with Eulerian and Lagrangian approaches, respectively. The discretization process for each phase is independent of each other and does not require body-fitted meshes. As illustrated in Figure 2 (a), two sets of discretizations are used: The Lagrangian points are attached to and stay on the outline of bed shape Γ. In contrast, the Eulerian mesh spans the whole domain, Ω_i, including the area occupied by the solid structure.

The general idea of IBM is to solve the ice governing equation (1) and (9) on a Eulerian grid imposed on the ice domain, Ω_i, with a correction on the ice-bedrock interface Γ at each intermediate time step to impose the boundary condition. Here, we use the direct forcing implementation of IBM (Uhlmann, 2005). The implementation is decomposed into four steps. First, advance the governing equations (10) to (12) for one pseudo time step forward without considering the submerged bedrock. We refer to this solution as the intermediate fields $u^{n+1/2}$ and $T^{n+1/2}$

$$\frac{u_i^{n+1/2} - u_i^n}{\Delta\tau_u} = \left(\frac{\partial \tau_{ij}}{\partial x_j}\right)^n - \left(\frac{\partial p}{\partial x_i}\right)^n + F_i, \tag{14}$$

$$\frac{T_i^{n+1/2} - T_i^n}{\Delta\tau_T} = -\frac{\partial T}{\partial t} - \left(u_i \frac{\partial T}{\partial x_i}\right)^n + \frac{1}{\rho c_p}\left(\frac{\partial}{\partial x_i}\left(\kappa \frac{\partial T}{\partial x_i}\right) + 2\tau_E \dot{\epsilon}_E f(T - T_m)\right)^n, \tag{15}$$

where the superscript n represents the current pseudo time step and $\Delta\tau$ represents the pseudo time step size.

Second, we use a regularized delta δ function (Peskin, 2002) to translate the intermediate quantities $u^{n+1/2}, T^{n+1/2}$ from the Eulerain points x to that on the Lagrangian

points X_l. Dropping the superscript for simplicity, we have

$$U(X_l) = \sum u(x)\delta(x - X_l)\mathrm{dxdz}, \quad Q(X_l) = \sum q(x)\delta(x - X_l)\mathrm{dxdz}, \tag{16}$$

where $q = \partial T/\partial x_i$ denotes the heat flux, dx and dz are the horizontal and vertical grid size, and the lower case and upper letters represent Eulerian and Lagrangian quantities, respectively. The delta function is a continuous differentiable function that takes 1 if the Eulerian grid point is on the Lagrangian point and 0 if far away, thus allowing a smooth transfer between the grids.

Third, we compute the volume forces F_U and F_Q required to achieve the desired boundary condition, in this case, the no-slip condition $U^d = 0$ and constant geothermal heating condition Q^d

$$\frac{U^{n+1/2} - U^d}{\Delta t} = F_U^{n+1/2}, \quad \frac{Q^{n+1/2} - Q^d}{\Delta t} = F_Q^{n+1/2}. \tag{17}$$

Finally, we use the computed volume force to correct the intermediate fields u and T and obtain the velocity and temperature fields at the next pseudo time step

$$u^{n+1} = u^{n+1/2} + \frac{F_U^{n+1/2}}{\Delta V_{lag}}, \quad q^{n+1} = q^{n+1/2} + \frac{F_Q^{n+1/2}}{\Delta V_{lag}}, \tag{18}$$

where ΔV_{lag} is control volume of one Lagrangian points. In our model, we select the number of Lagrangian points such that $\Delta V_{\mathrm{lag}} \sim \mathrm{dxdz}$.

The other interface that requires careful numerical treatment is the upper surface of the ice. Ice thins as it speeds up and the free surface moves downwards towards the bed. While the movement itself is relatively slow and gradual, its thermal implications could be very important (e.g., Mantelli et al., 2019). To capture ice thinning, we represent the free surface as the level-set of a higher dimensional distance function, as illustrated in Figure 2 (b), allowing us to handle the moving front implicitly as discussed in the books by Sethian (1999) and Osher et al. (2004). More specifically, the ice-air interface is defined as the zero-contour of a signed distance function ϕ

$$\phi(x) = \begin{cases} -d & \text{if } x \in \text{air}, \\ +d & \text{if } x \in \text{ice}. \\ 0 & \text{if } x \in \Gamma, \end{cases} \tag{19}$$

where d is the distance from the grid point to the interface. Across $\phi(x) = 0$, the density ρ, viscosity η, and thermal conductivity κ change

$$\rho(\phi) = \rho_a + (\rho_i - \rho_a)H(\phi), \tag{20}$$

$$\eta(\phi) = \eta_a + (\eta_i - \eta_a)H(\phi), \tag{21}$$

$$\kappa(\phi) = \kappa_a + (\kappa_i - \kappa_a)H(\phi), \tag{22}$$

where the subscript i denotes the material properties in the ice domain, subscript a denotes those in the air domain, and H is the Heaviside function defined as

$$H(\phi) = \begin{cases} 0 & \phi < -\epsilon, \\ \frac{1}{2} + \frac{\phi}{2\epsilon} + \frac{1}{2\pi}\sin\frac{\pi\phi}{\epsilon} & -\epsilon \le \phi \le \epsilon, \\ 1 & \phi > \epsilon, \end{cases} \tag{23}$$

with a smoothing length of $\epsilon = 3\Delta x$ (Sethian, 1999; Sethian & Smereka, 2003).

To evolve the location of the interface, we advect the level field using the general advection equation, also known as the level-set equation:

$$\frac{\partial \phi}{\partial t} + u_n|\nabla\phi| = 0, \tag{24}$$

where u_n is the physical velocity in the normal direction of the ice surface. This equation moves the implicit front with the ice velocity field determined by the mechanical equation (1) at each physical time step. The spatial discretizations use first-order upwind, and the temporal discretizations use the second-order accurate Total Variation Diminishing Runge–Kutta schemes. Since the ice-air interface remains smooth at all times and thins only slightly as compared to the overall thickness of the ice sheet, sophisticated advection schemes such as extension velocities (Adalsteinsson & Sethian, 1999), topology-preservation techniques (Qin et al., 2015) or reinitialization (Osher et al., 2004) are not necessary in our case.

2.3 Verification

To verify the accuracy of our numerical method, we compare our numerical results to two analytical solutions: the circular inclusion test (Schmid & Podladchikov, 2003) and the classic Nye solution for the velocity field in ice flowing over a wavy surface (Nye, 1969). These two benchmarks are complementary, because the circular-inclusion test is better suited for identifying spurious oscillations in the pressure field while the Nye solution represents a flow configuration more closely related to the dynamic problem we aim to understand.

Following Schmid and Podladchikov (2003), we consider a circular solid inclusion immersed in a square domain with homogeneous fluid. We apply a pure shear boundary condition to the fluid domain and a no-slip to inclusion-fluid boundary. To evaluate the accuracy of the numerical scheme, we compare our numerical results to the analytical solutions of the pressure and velocity fields

$$v_x + iv_y = \epsilon R^2(-\frac{1}{z} - \frac{z^3}{r^4} + R^2\frac{z^3}{r^6}) + \dot{\epsilon}\frac{r^2}{z}, \tag{25}$$

$$P = 4\eta\epsilon\cos(2\theta)\frac{R^2}{r^2}, \tag{26}$$

where $z = x+iy = re^{i\theta}$, ϵ is the shear strain rate, η is the fluid viscosity and R is the radius of the inclusion. The boundary conditions applied are the pure shear strain rate

$$v_x = \dot{\epsilon}x, v_y = -\dot{\epsilon}y. \tag{27}$$

Figure 3 depicts the spatial convergences for the inclusion case, where (b) and (c) compare the results of numerical and analytical vertical velocity fields, (d) and (e) compare the results of pressure fields, and (a) shows that the combination of the Stokes solver and IBM leads to the spatial accuracy around order 1.5.

We further test our model with Nye's analysis of the flow over wavy bed with a Newtonian fluid. We followed Nye (1969)'s model setting, and considered the bed shape in the form of a sine wave $z_0 = \epsilon a\sin(kx)$. The boundary condition is simple shear on the surface $(\tau_x, \tau_z) = (1, 0)$, periodic in the flow direction. Here, we limit our reference analytical solution to only first order $\mathcal{O}(\epsilon)$

$$u = U\left(1 + z\epsilon a\beta k^2\exp(-kz)\sin(kx)\right) + \mathcal{O}(\epsilon^2), \tag{28}$$

$$v = U\epsilon a\beta k(1+kz)\exp(-kz)\cos(kx) + \mathcal{O}(\epsilon^2), \tag{29}$$

$$p = 2\epsilon\eta U a\beta k^2\exp(-kz)\cos(kx) + \mathcal{O}(\epsilon^2), \tag{30}$$

where U is the far field horizontal velocity, $\beta = k_*^2/(k_*^2 + k^2)$, and k_* stands for the characteristic wavenumber of regelation. The full solution can be found in Nye (1969).

Figures 4 (b-c) show the comparison between the numerical and analytical vertical velocity fields. In (d), we show the pressure comparison along the $z = 2.2$ m horizontal line. It should be noted here that the analytical solutions we compare to is only to the first order. This is the reason for the observed slight discrepancies between the two solutions in the peak and low regions in panel (c). Panel (a) shows that the spatial accuracy of IBM and spatial solver together is around order of 1.5.

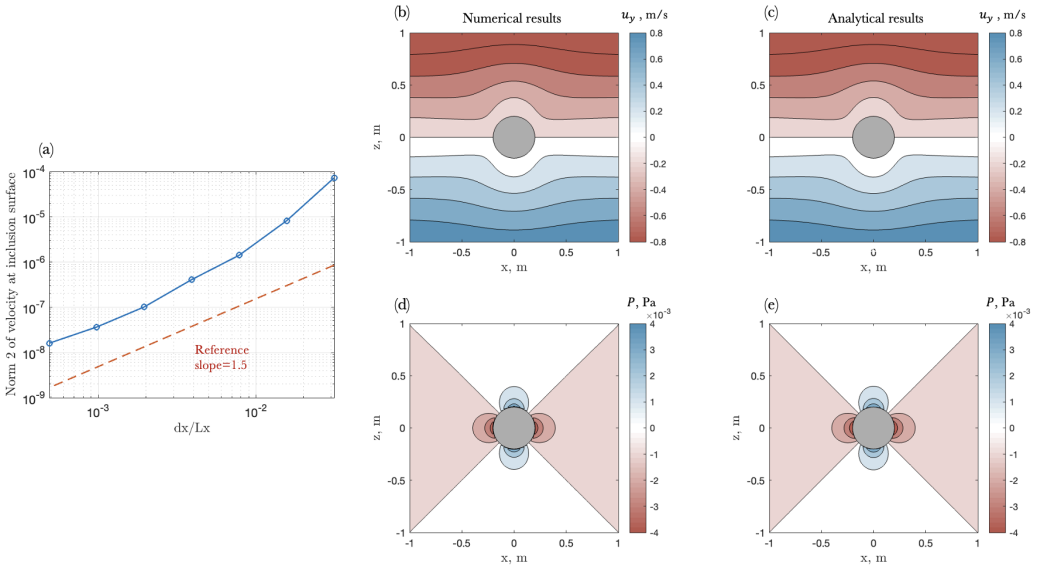

Figure 3. Spatial convergence test for the inclusion case . (a): L2 norm of the velocity at the cylinder. (b) and (c): Vertical velocity in the analytical case and numerical case, respectively. The black slid lines in (b) and (c) represent the streamlines. (d) and (e): Pressure in the analytical case and numerical case, respectively. The resolution shown here is 512 x 512.

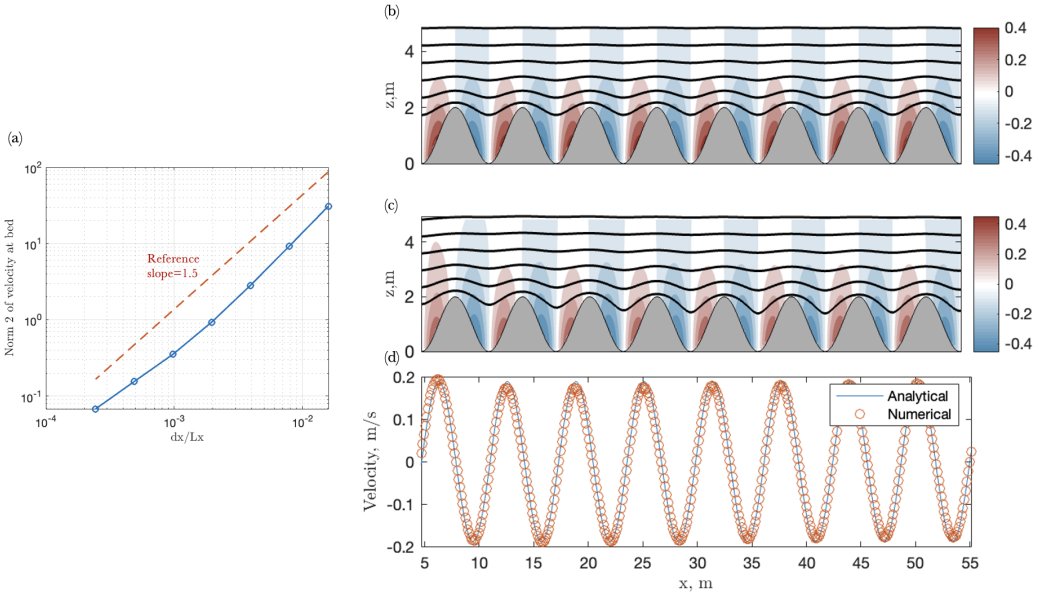

Figure 4. Comparison of numerical solutions against analytical solutions of Nye's problem (Nye, 1969). (a): L2 norm of the velocity at the bed. (b) and (c): Vertical velocity for the analytical and numerical case, respectively. The black slid lines in (b) and (c) represent the streamlines. (d): Pressure along the $z = 2.2$ m for both numerical and anlytical cases. The resolution shown here is 512 x 128.

3 Results

We set our simulation domain size to 4800 m by 800 m across all simulations in this section. The surface temperature used in the simulations is prescribed as -26°C as a rep-

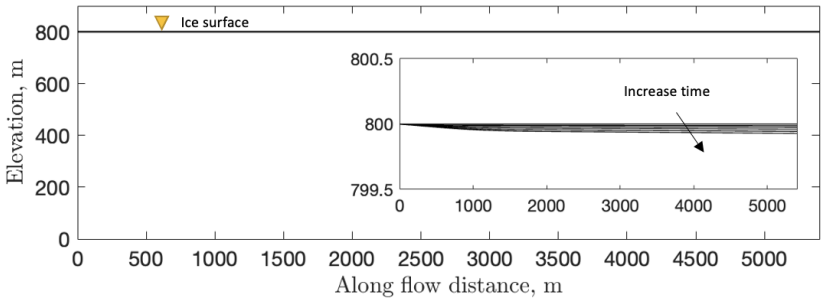

Figure 5. Ice surface evolution over 80 years on a flat bed. The sub-panel shows a zoom-in view of the ice surface evolution.

resentative value for the surface temperature in Antarctica. Additionally, we apply a geothermal heat flux of 0.05W/m^2 (Wright et al., 2012; Shapiro & Ritzwoller, 2004; Maule et al., 2005). The basal topography is modeled as $z_b = A\sin(kx)$, with an amplitude of $A = 100$ m and a wavenumber k ranging from 0.52 to 6.28.

For all simulations, we assume no-slip at the bed and a free surface. One example of the ice surface evolving over time is shown in Figure 5. At the scale of the model domain, the ice-surface change is not immediately apparent, but a close-up view of the upper tens of meters of the domain clarifies that the surface is evolving if only by a few meters or less than 1% of the ice thickness. Given this small change and our focus on shear localization near the bed, we only plot the bottom part of our model domain in the remaining figures of this section.

3.1 Ice Flowing over Topography May Form an Internal Shear Band

To identify how basal topography affects internal deformation, we compare the thermomechanical deformation of ice flowing over an idealized sinusoidal topography to ice flowing without topographic control (Figure 6). All other parameters and boundary conditions are identical for the two cases. Here we use the the power-law rheology with the exponent $n = 3$ (Glen, 1952, 1955) and include water weakening in the effective viscosity as discussed in Section 2.1.

Figure 6 (a) shows the case of ice (light blue) flowing over a sinusoidal topography (dark grey) for the lower portion of our model domain. The ice speeds up from left to right as indicated by the green velocity profiles at four different along-flow locations of $x = 536, 1854, 3162, 4235$ m, where we compare the local velocity in dark green with inflow velocity in light green. This speed-up is facilitated by shear localizing $dudz$ increasingly on top of the topography as indicated in blue. The highest shear values occur on the topographic highs, effectively linking these up into a continuous zone of elevated shear strain rate. The control simulation of ice flowing over a flat topography is shown in Figure 6 (b). Similarly to Figure 6 (a), ice speeds up as it flows downstream, aided by shear strain rate in the immediate vicinity of the flat topography.

The main difference between the two simulations is how shear strain rate is distributed with depth (Figure 6, c). For the flat bed (Figure 6, b), the shear strain rate is highest nearest to the bed, whereas topography shifts the shear-rate maximum into the ice column to a depth that is corresponds roughly to the height of the topographic peaks (Figure 6, a). Both modes of deformation are capable of generating approximately comparable surface speeds of around 70 m/yr, with the ice flowing over rough topography moving slightly faster at equal driving stress and basal resistance. Since the speed-up of the

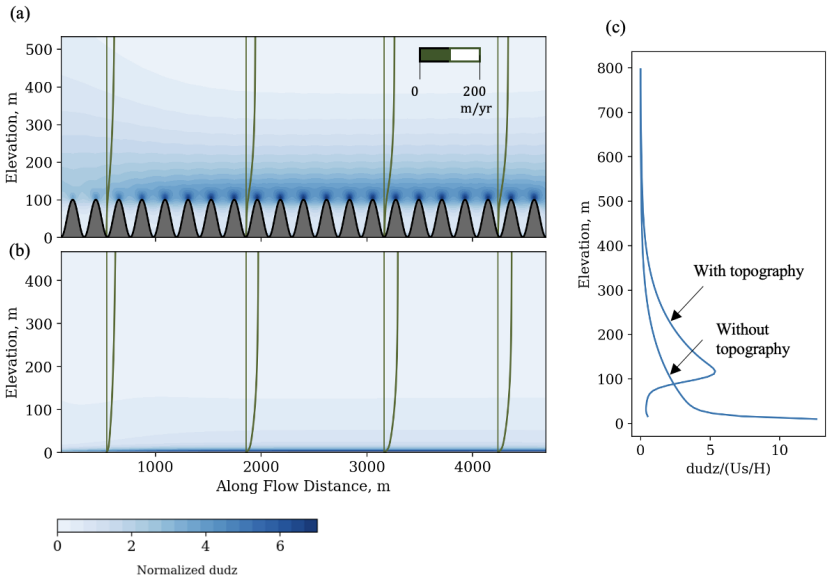

Figure 6. Role of basal topography in shear localization. (a) and (b): Shear strain rate $\partial u/\partial z$ in the background contour for the case of with basal topography and without basal topography. The velocity profiles at different locations along the flow are shown in the dark green lines, with a reference inflow velocity in light green lines. (c): Shear strain rate profile at $x = 4235$ m for both cases.

ice is gradual and not instantaneous, the cooling effect associated with ice thinning is not sufficient to prevent viscosity weakening in either of the simulations.

To quantify the share of total deformation accommodated within the ice as ice flows over the basal topography, we define $\tilde{R}_d$ as the percentage of the internal deformation in the ice column to be the ratio of the integral of the shear strain rate from the bed up to some elevation z and the integral of the total shear strain rate in the entire ice column

$$\tilde{R}_d = \frac{\int_{\mathrm{b}}^{z} \frac{\partial u}{\partial z}}{\int_{\mathrm{b}}^{\mathrm{s}} \frac{\partial u}{\partial z}} = \frac{u_z}{U_{\mathrm{s}}}, \tag{31}$$

where subscripts d, b and s represent deformation, bed and surface, respectively. The tilde denotes a non-dimensional parameter. This parameter can also be interpreted as the velocity ratio: local x velocity divided by the surface x velocity in the same ice column.

We use the term "shear band" to be a basal zone that accommodates the majority ($\geq 50\%$) of the total deformation in the ice column. We set the lower and upper bound of the internal shear band $\tilde{R}_{dl}$ and $\tilde{R}_{du}$ to 20% and 70%, respectively. Finally, we define the bandwidth B_w as the vertical distance between these two bounds

$$B_w = z(\tilde{R}_{du}) - z(\tilde{R}_{dl}) \ . \tag{32}$$

Figure 7 shows how the shear band evolves within the model domain. Towards the left boundary, deformation is distributed relatively evenly as indicated by the 20% and 70% contour differing by several hundred meters in depth (Figure 7, a). As ice flows downstream, the lower limit of the shear band, $\tilde{R}_{dl} = 20\%$, stays on top of the basal topography shape and does not change depth much. This result highlights that the depth-distribution of deformation below the topographic highs remains relatively unaffected by the shear localization and ice speeds up mainly at and above the topographic highs. The upper

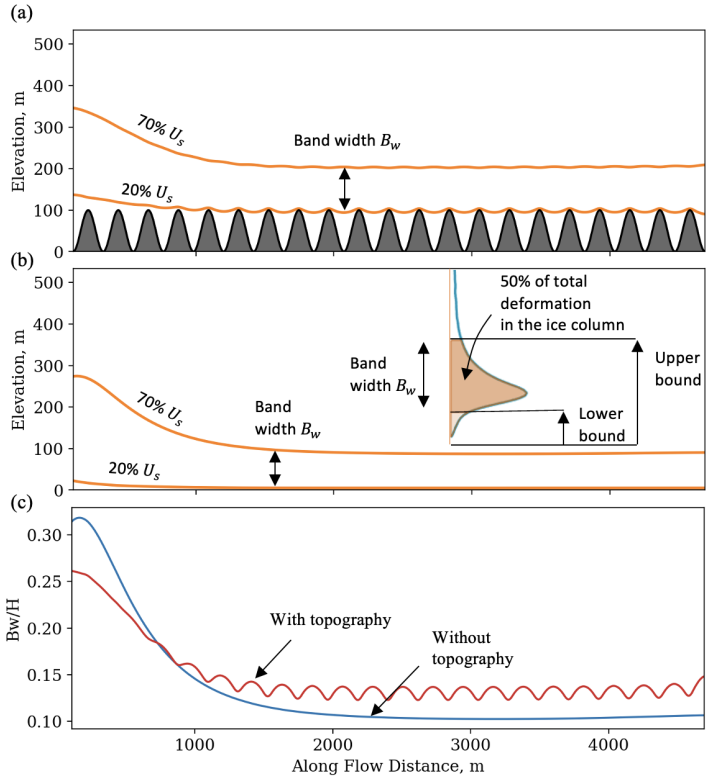

Figure 7. Shear band development along the flow. (a) and (b): Shear band development with and without a topography, defined as a basal zone where the 50% of total deformation in the ice column occurs. We define the lower and upper boundary of the shear band to be 20% and 70% of the deformation in the ice column, as illustrated in the sub-panel in (b). (c): Ratio of the shear band bandwidth B_w to the ice thickness H at that location along the flow for both cases.

limit $\tilde{R}_{du} = 70\%$ descends sharply, and then stabilizes around $z = 200$ m. For the case shown, the shear band has a width that is close to the amplitude of the sinusoidal bed shape, and accommodates approximately half of the total shear strain rate.

In the control case without topography, deformation also localizes due to viscosity weakening, but the shear band is located at the bed instead of within the ice column. The shear strain rate is maximal at the ice-bedrock interface with the $\tilde{R}_{dl} = 20\%$ contour remaining very close to and almost at the bed (Figure 7, b). Figure 7 (c) shows the ratio of the shear band bandwidth B_w to the ice thickness H. Initially, the shear band width constitutes about 30% of the ice thickness for both cases. It decreases rapidly in the downstream direction, and finally stabilizes at a width of approximately 10% of the ice thickness.

3.2 Shear Band Formation is The Consequence of a Positive Energy Budget Near Topographic Peaks

Similar to the creep instability, shear band formation is driven by the positive feedback that localized deformation reduces ice viscosity that further localizes deformation. This feedback depends on the degree to which ice in the vicinity of topographic highs warms up during flow, as captured in the energy equation (9). Three terms contribute to the thermal evolution: advection, diffusion, and shear heating. Through a simple scal-

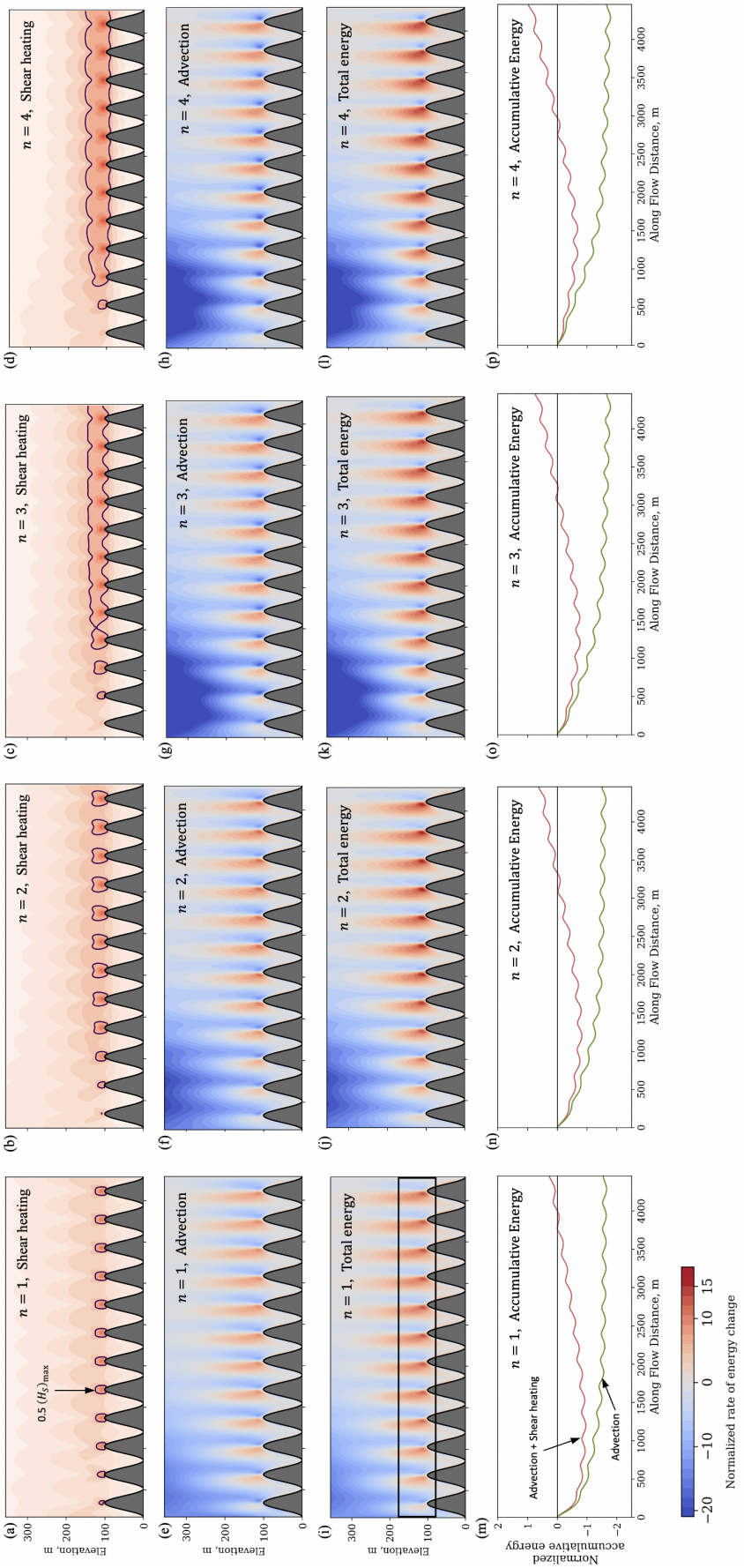

Figure 8. Role of the power-law exponent n on normalized shear heating $\widetilde{H}_s$, vertical advection $\widetilde{A}_v$, and approximated total energy $\widetilde{E}$ as defined in equation (33). First row (a-d): Normalized shear heating $\widetilde{H}_s$ contours in $x - z$ domain. The black contour lines denotes half of the maximum of $\widetilde{H}_s$, in this case 3.15. Second row (e-h): Normalized vertical advection $\widetilde{A}_v$ contours. Third row (i-l): Normalized approximated total energy $\widetilde{E} = \widetilde{H}_s + \widetilde{A}_v$ contours. Fourth row (m-p): Depth averaged accumulative total energy (red curves) and accumulative vertical advection (green curves) along x axis. The averaged area is indicated as the black box from $z = 80 - 180$ m in (i). Each column represents a different value of n as indicated in all panels. All simulations have the same basal topography of $Ak = 1.83$, where Ak is defined as the product of amplitude and wavenumber of the bed.

ing analysis (see Appendix A), we find that vertical advection and shear heating are the two primary competing terms in our case. In comparison, diffusion is roughly two orders of magnitude smaller than these two terms. Therefore, we approximate the total energy as the combined contributions of only vertical advection and shear heating.

To meaningfully compare the magnitude of advection and shear heating for different n from 1 to 4, we first divide the shear heating term $2\tau_E\dot{\epsilon}$ by ρc_p to ensure that both terms have the same units of K/s. We then normalize both terms using the characteristic shear heating $\rho g U_s \sin\alpha$, which represents the magnitude of shear heating at the bed, assuming that the x velocity varies linearly with depth. The non-dimensional advection and shear heating terms can be then expressed as

$$\widetilde{H}_s = \frac{2\tau_E\dot{\epsilon}}{\rho g U_s \sin\alpha}, \quad \widetilde{A}_v = \frac{\partial T}{\partial z}\frac{u_z c_p}{g U_s \sin\alpha}, \tag{33}$$

where H_s is shear heating, A_v is vertical advection, U_s is the surface speed, u_z is the vertical velocity, and tilde represent non-dimensional quantities. Figure 8 compares the rate of normalized energy change attributed only to shear heating (first row), vertical advection (second row), and the approximated total energy (third row) for values of n ranging from 1 to 4 (column 1 to 4). We plot the energy change over time on the same color scale for the first three rows for easier comparison.

In Figures 8 (a-d), the black contour lines highlight half of the maximum shear heating value ($\widetilde{H}_s = 3.15$). The heating is positive throughout the domain and concentrates within the internal shear band extending on top of topographic highs. The rate of heating tends to increase in the downstream direction. Notably, for $n = 1$, shear heating on topographic highs is minimal. As the value of n increases, these localized shear heating regions begin to connect and form a band situated above the topography. For example, in Figure 8, zones of elevated shear heating begin to bridge when $n \geq 3$.

The primary effect of vertical advection is cooling (Figures 8, e-h). Particularly in the left third of the domain where cold ice is drawn down from the surface. This cooling effect is also reflected in the dipping of the iso-velocity-ratio lines in Figures C1 and C2. In the immediate vicinity of topographic highs, however, vertical advection is positive in the windward side of the obstacle and negative on the lee side, as evidenced by the alternating blue and red regions.

Summing shear heating and vertical advection produces the approximate total energy, indicative of the energy budget of the basal ice (Figures 8, i-l). The impact of shear heating is primarily confined to the vicinity of the basal topography, as deformation is predominantly concentrated near the bed. However, upon closer examination, it becomes evident that the lee side of the bumps, characterized by negative advection, is partially balanced by shear heating. The windward side of the bumps, dominated by positive advection, experiences reinforcement.

We calculate the depth-averaged accumulative quantities for total energy and vertical advection within the specified range from z_1 to z_2, as indicated by the black box in (i)

$$\overline{\widetilde{H}}_s(x) = \int_0^x \frac{1}{z_2 - z_1}\int_{z_1}^{z_2} \widetilde{H}_s dz dx, \quad \overline{\widetilde{A}}_v(x) = \int_0^x \frac{1}{z_2 - z_1}\int_{z_1}^{z_2} \widetilde{A}_v dz dx. \tag{34}$$

This cumulative measure serves as an indicator of the energy carried by the ice as it flows downstream. To focus on the basal region of interest, we select a depth-averaged range of 80-180 m, setting the interval to align with the amplitude of the sinusoidal bed.

Figures 8 (m-p) depict the cumulative energy profiles, where the green curves represent $\overline{\widetilde{A}}_v$, considering only vertical advection, and the red curves represent $\overline{\widetilde{E}}$, considering both vertical advection and shear heating. $\overline{\widetilde{A}}_v$ consistently exhibits negative values for all values of n, indicating that the ice within the basal region does not experi-

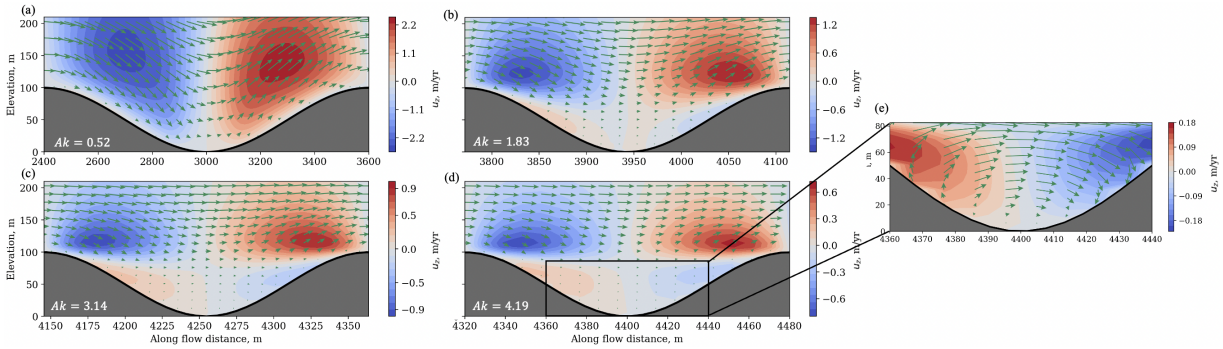

Figure 9. Role of basal topography shape in flow separation for $n = 3$. Each panel presents the vertical velocity contours and velocity vectors corresponding to a specific value of Ak, namely 0.52 (a), 1.83 (b), 3.14 (c), and 4.19 (d). (e) shows a zoomed-in perspective of the bottom of trough of (d).

ence positive energy gain. However, upon incorporating shear heating alongside vertical advection, $\widetilde{\widetilde{E}}$ gradually becomes positive in the downstream direction. This trend holds true across all values of n, although higher values of n tend to amplify the extent of cumulative total energy.

One important implication of shear band formation as shown in Figures 8 (e-h) is a separation of the flow in the ice: The ice above the shear-bank moves relatively fast and is characterized by a simple flow field dominated by speed-up in the flow direction. In contrast, basal ice slows down as the shear band accommodates the majority of the deformation. The flow field in the basal ice underneath the shear band is more complex. Figure 9 shows how the degree of flow separation varies for four different topographies defined by the shape factor Ak that represents the product of amplitude and wavelength of the bed. We show the flow field only for a single trough with shape factors Ak of 0.52, 1.83, 3.14, and 4.19 for a rheological power-law exponent of $n = 3$.

For a relatively low value of Ak (Figure 9, a), ice follows the downhill and uphill contours of the topography, maintaining a smooth flow. As Ak increases to 1.83 (Figure 9, b), at the bottom of the trough there is a slight upward flow near the bed on the downhill side and a downward flow on the uphill side, indicating the onset of separation. As Ak continues to rise (Figures 9, c-e), this trend becomes more pronounced. Between the bumps, four distinct regions emerge: Above the peak of topography, the flow still exhibits the characteristic down-up motion. Below the peak, the flow in the trough reverses its direction, moving back from the uphill side of the next bump to the downhill side of the previous bump (Figure 9, e).

The separation line, which marks the division of flow, is positioned slightly below the peak of the topography. In the case of $A = 100$ m, the separation line is approximately located at $z = 80$ m. The occurrence of flow separation is important because it leads to a division of the flow in the vertical direction. The presence of flow separation could hence be an indicator for the existence of an internal shear band. The lower portion experiences relatively slow, re-circulatory motion ($u <\sim 0.2$ m/yr). In contrast, the upper portion flows over a bed that "appears smoother" than its actual shape. Consequently, when flow separation occurs, the ice situated above the basal topography may not feel the complete underlying bed shape.

3.3 Scaling of Internal Shear Band Formation Using Topography and Rheology parameters

In Sections 3.1 and 3.2, we found that shear heating can dominate over advection near topographic peaks, leading to a net increase in energy budget in basal ice. The internal shear band development depends not only on power-law-exponent n, but also on the shape of the sinusoidal topography Ak. In this section, we aim to understand the dual effect of these two parameters and quantify their role in inducing shear localization through scaling analysis and numerical simulations.

For our scaling analysis, we consider a steady state internal shear band under a specific sinusoidal shape characterized by Ak and rheology exponent n. We assume that the ice flow is fully developed in x direction, thus all $\partial/\partial x$ becomes zero. The momentum equation in x direction can then be simplified to

$$\frac{\partial(\eta\epsilon_{xx})}{\partial x} + \frac{\partial(\eta\epsilon_{xz})}{\partial z} \quad = \quad -\rho g \sin\alpha. \tag{35}$$

We impose a generic power-law rheology without temperature dependence and assume the main stress component is the shear stress, i.e., $\tau_E \approx \tau_{xz}$. The viscosity has the following form

$$\eta = \frac{1}{2} a_0^{-\frac{1}{n}} \left(\frac{\partial u}{\partial z}\right)^{-1+\frac{1}{n}}. \tag{36}$$

For the sinusoidal topography, we choose the characteristic horizontal length l to be $\sim \lambda^{(n-1)p} A^{1-(n-1)p}$, where p is some constant and n is the power-low exponent. We choose this the exponent such that the characteristic horizontal length scale have the same unit as length, and we choose $(n-1)$ to avoid zero denominator in the later derivation. After substituting all of these into the momentum equation and with the relationship $Ak = 2\pi A/\lambda$, we have

$$B_w \propto (Ak)^{-2pn}. \tag{37}$$

For a more detailed derivation, please refer to Appendix B.

To test the derived scaling relationship against our simulations, we conduct four sets of numerical experiments with $n = 1, 2, 3, 4$. We include a range of shape factor Ak values spanning from 0.52 to 6.28. Shape factor $Ak = 0.52$ corresponds to wavelength is 16 times larger than amplitude, and $Ak = 6.28$ corresponds to the scenario where the amplitude of the bump matches the wavelength. Figure 10 shows *dudz* variations with different exponent n and shape factor Ak. Here, we normalize the absolute value *dudz* by U_s/H where U_s is the surface speed and H is the ice thickness for better comparison across different Ak and n.

The influence of Ak on shear localization and shear band forming is similar across all n. When Ak is low (Figures 10, a-d), shear deformation *dudz* is concentrated around the topographic peaks. As Ak increases, *dudz* localization on the peaks begins to connect and bridges as anticipated, e.g. Figures 10 (c,g,k). When Ak is approximately 2 or larger, the shape of the $70\,\%U_s$ and $20\,\%U_s$ contour lines, depicted in solid orange lines in all panels, become less wiggle and no longer align with the underlying shape of the basal topography (Figures 10, j-l). Accordingly, the bandwidth stabilizes with fewer oscillations (Figures 10, n-p).

The relationship between B_w/H, Ak and n is depicted in Figure 11. Each marker represents a normalized bandwidth value corresponding to a specific shape factor and exponent from the simulations. To determine the stabilized bandwidth, we compute the average bandwidth value across three consecutive bumps in the downstream region of the domain. We exclude the upstream part from the averaging process due to the ongoing rapid thinning of the ice, which could lead to an overestimation of the bandwidth.

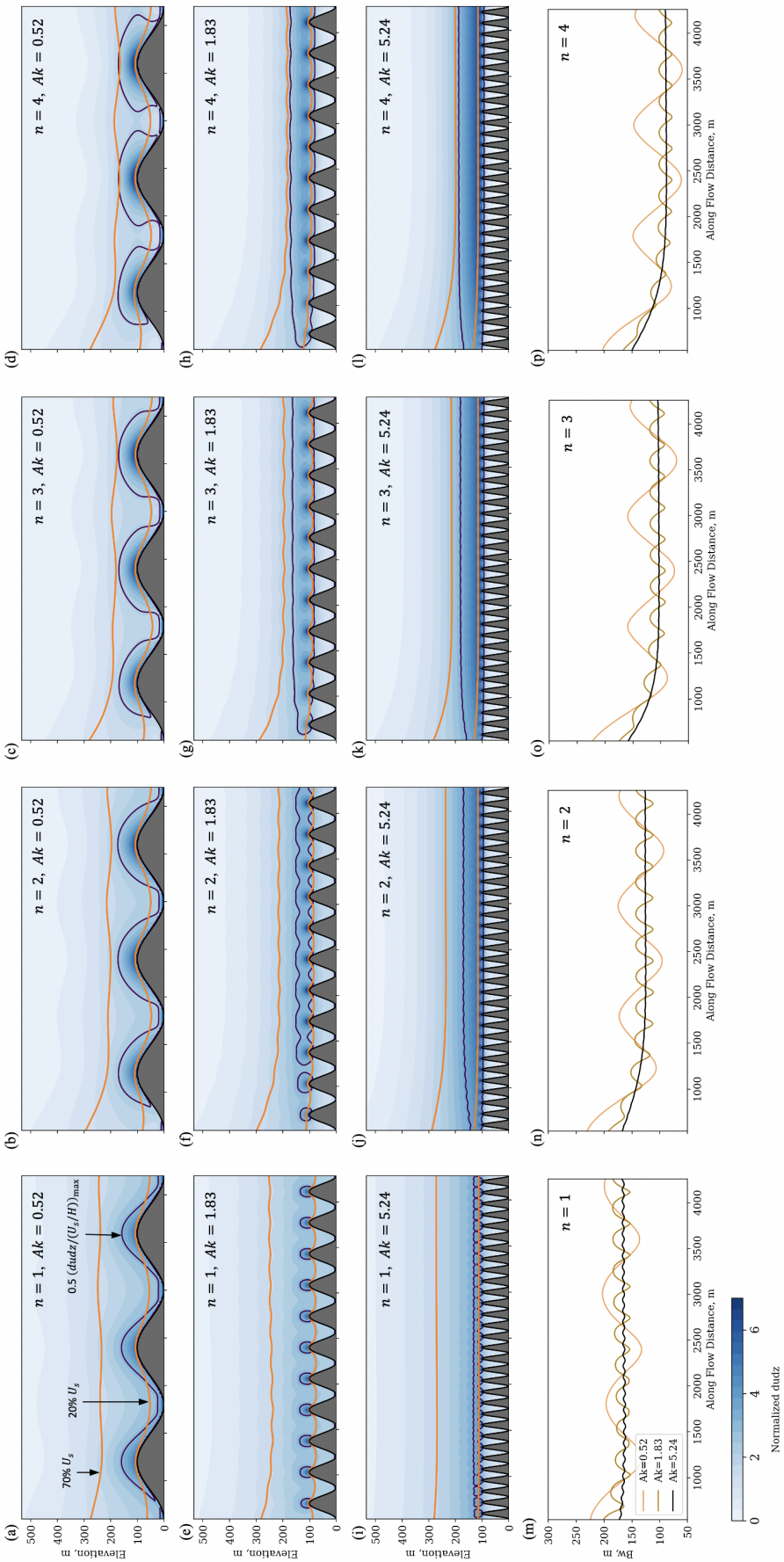

Figure 10. The normalized deformation $dudz$ variations with different exponent n and shape factor Ak. The first three rows corresponds to shape factors $Ak = 0.52$ (a-d), 1.83 (e-h), and 5.24 (i-l), respectively. Each column represents a specific value of the exponent n. In the first three rows of each panel, the two orange lines indicate the contours of 70% U_s and 20% U_s as defined in equation (31) and illustrated in Figure 7. The black contour in the first 3 rows in each panel highlights half of the maximum value of $dudz/(U_s/H)$, in this case 3.15. The last row (m-p) show how the thickness of the bandwidth, defined as the vertical distance between 70% U_s and 20% U_s lines, varies along the flow for different shape factors and exponents.

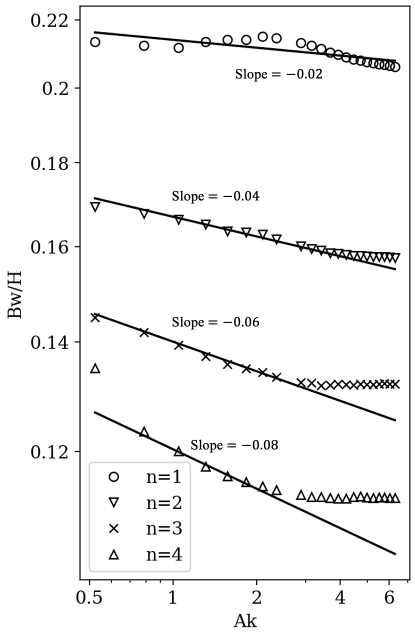

Figure 11. The regime diagram of the internal shear bandwidth B_w/H, power-law exponent n, and shape factor Ak of the sinusoidal bed. Each marker shape corresponds to a distinct simulation set sharing the same n value, and each individual marker represents a single simulation.

In cases where the Ak value is too small to achieve three consecutive stable bumps, we adjust the number of averaged bumps accordingly. The selection of the averaging area is outlined in Figures C1 and C2.

Observing the gradual increase in Ak, we note a corresponding decrease trend in the width of the internal shear band for all n. The rate of this decrease varies, with a slope of the logscaled relationship approximately following a pattern of $-0.02n$. This suggests that for larger values of n, the width of the shear band reduce at a faster rate, thus localizing the deformation significantly more. It is evident that when Ak continues to increase, the averaged bandwidth eventually stabilizes around a certain value (Figure 11 down-triangle, cross, and up-triangle markers). This critical Ak value at which the width stabilizes decreases as n increases. Specifically, we observe that the widths stabilize around $Ak = 4.45,\ 3.14,\ 2.62$ for $n = 2, 3, 4$ respectively. However, this trend is less pronounced for $n = 1$. Even at the most rugged topography considered, where the amplitude equals the wavelength, a stable width of the shear band is still not observed (Figure 11 circle markers).

By varying the basal topography shape factor Ak and exponent n, we can conclude from the numerical experiments that for each exponent n, there exist a steady state shear band width as $Ak \to \infty$ (Figure 11). When Ak is high, the velocity ratio contours tend to concentrate at a consistent elevation and do not align with the shape of the basal topography (Figures C1 and C2). This suggests that the perturbations originating from the basal topography propagate upwards from the bed to the surface only over distances spanning tens to a few hundred meters, depending on the value of n. Thus, the influence of the actual basal topography shape on the internal ice above this level is likely reduced, and the internal ice progressively "perceives less" of the specific shapes of the basal topography.

The scaling relationship between the bandwidth and non-dimensional shape factor Ak raised to the power of $-2pn$ is shown as the solid lines in Figure 11. From the simulation results, we infer that the value of p takes around 0.01. Before the width of the shear band stabilizes, thescaling of $-2pn$ captures the decreasing rate very well. Yet it is important to acknowledge that this scaling relationship does not account for the influence of temperature-dependent rheology and flow variations in the x direction (i.e., assume fully developed flow). Consequently, the aforementioned relationship tends to slightly underestimate the actual degree of localization.

As the spacing between two bumps approaches infinitesimally small values ($Ak \rightarrow \infty$), scaling suggests B_w tends towards zero, which is physically unrealistic. A zero thickness for the internal shear band implies the presence of internal "slip" where velocity becomes discontinuous. Since our model focuses on understanding flow localization, it does not permit a discontinuities in velocity anywhere in the computational domain. Hence, as $Ak \rightarrow \infty$, we anticipate that B_w will stabilize after surpassing a specific Ak value, indicating that the thickness of the internal shear band has reached its minimum possible value for a given n.

4 Discussion

The fast speed of many glaciers and ice streams are thought to be accommodated by basal sliding with internal deformation contributing only minimally (Echelmeyer & Zhongxiang, 1987; Hermann & Barclay, 1998; Rignot et al., 2011; Rignot & Mouginot, 2012). However, recent advances in our understanding of the different deformational regime of ice particularly at high stresses (Goldsby & Kohlstedt, 2001), a growing appreciation for the sharp weakening of ice near pre-melting conditions (Krabbendam, 2016), and field evidence of complex, depth-dependent deformation in fast-moving ice (Law et al., 2023; Maier et al., 2019; Hills et al., 2017) merit a re-evaluation of the degree to which internal deformation may contribute to fast ice motion.

In the presence of complex basal topography, internal deformation may actually have more localization than usually expected when most glacier models tend to use a smooth bed due to the bed resolution limitation (Law et al., 2023). While Law et al. (2023) focuses more on descriptive aspects of ice motion at specific field sites, our study complements the finding of spatially variable deformation along depth by bringing in an in-depth analysis of two physical processes that contribute to this spontaneously formed localization: vertical advection and shear heating. We show that vertical advection is proportional to the rate of thinning and therefore the rate of glacier acceleration. When shear heating dominates over the vertical advection, the net energy gain in the shear band region becomes positive and provides a necessary condition for an internal shear band to form. Otherwise, when net energy gain is negative or oscillates around a very small value, and shear band formation is suppressed. The accumulative approximated total energy, defined as the sum of shear heating and vertical advection, grows with increasing nonlinearity in ice rheology, captured by the power-law exponent n, for a given topography.

Basal topography amplifies shear heating, because it causes additional deformation within the ice. Importantly, this deformation is not reduced but instead amplified by speed-up as ice is forced to wrap around topographic highs at increasing speed. We emphasize that the high-degree of shear localization occurring within an internal shear band does not represent sliding. In our simulations, ice is frozen to the bed while an internal shear band forms above it, creating flow separation between the slow-moving ice trapped in topographic troughs and the fast-moving ice above the internal shear band. As speed-up continues, it is possible that the ice underneath the internal shear band gradually warms and becomes temperate. The existence of temperate zones with variable ver-

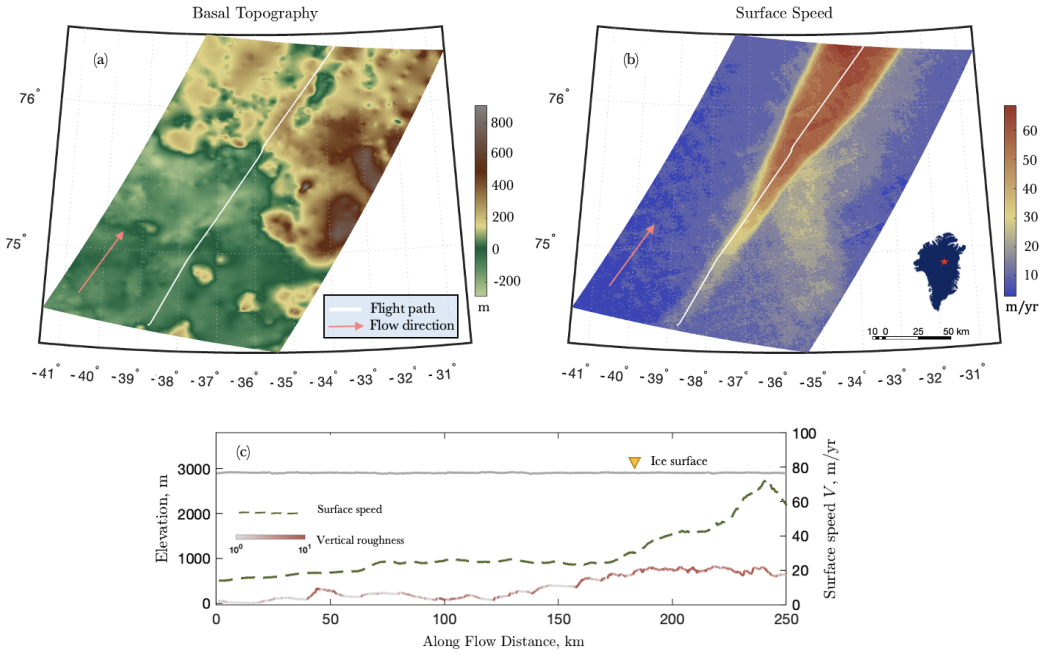

Figure 12. Basal topography and surface speed at NEGIS. (a): basal topography contour from BedMachine 3 (Morlighem et al., 2017). (b): surface speed contour from MEaSUREs NSIDC (Joughin et al., 2015). (c): surface speed (dashed line) change with the basal topography (black solid line) along flight path, indicated as the white lines in (a) and (b). The ice surface is shown as a grey solid line. The basal topography and ice thickness in (c) is obtained from Franke et al. (2021).

tical extent depending on topography is supported by borehole data (Harrington et al., 2015; Hills et al., 2017; Law et al., 2023).

Our simulations demonstrate that the speed-up associated with the formation of an internal shear band is gradual in the sense that it develops over spatial scales larger than the ice-thickness. In field settings where an increase in ice surface speed appears to correlate with a change in basal roughness, speed-up tends to occur on a similar scale of multiple ice thickness, such as the Northeast Greenland Ice Stream (NEGIS) (Bamber et al., 2001), the Siple Coast Ice Streams (Siegert et al., 2004), and the Institute Ice Stream (Bingham & Siegert, 2007). For example, Figure 12 shows that the basal topography at NEGIS becomes more pronounced in the flow direction (Figure 12, a) and that the surface speed increases as the ice stream broadens (Figure 12, b).

We show the NEGIS example here merely to demonstrate that the type of dynamics identifies in our idealized simulations could have ramifications for understanding ice dynamics in specific field settings. It is an interesting example for shedding light on the relevant scales contributing to ice speed-up: The spatial scale over which topographic peaks vary prior to 170 km downstream is tens of meters (Figure 12, a). This scale is small as compared to the ice thickness of several hundred meters, but larger than the small-scale roughness of a few meters considered in existing sliding laws (e.g., Weertman, 1957; Nye, 1959; Lliboutry, 1968; Fowler, 2010; Schoof, 2005; Bindschadler, 2006; Petrat et al., 2012). As a consequence, these intermediate scales are challenging to capture in large ice-sheet models. One contribution of our work is to advance our understanding and ability to capture the ice-dynamics implications of these intermediate-scale topo-

graphic variations in ice-sheet models, for example by smearing out the transition from flow-to-sliding over this scale (Bueler, 2009). Figure 12 exemplifies an interesting correlation between basal topography and surface speed, but it would be challenging to our model results against this data alone, because it does not constrain the potentially complex, depth-dependence of deformation within the ice.

A more direct comparison are borehole measurements of ice properties with depth. For example, Maier et al. (2019) drilled a network of eight boreholes at a slowly moving ridge located 33 km from the terminus of Issunguata Sermia within the ablation zone of the western margin of the Greenland Ice Sheet. Their measurements show a high shear strain rate concentrated within around $10 - 50$ m above the bedrock, but nearly zero shear strain rate is observed at bedrock. Such a high localization of shear strain rate in the interior of the ice evinces the possibility of internal sliding interface. The data indicates a pronounced increase in shear strain rate at an elevation of tens of meters above the bed followed by a rapid decrease in shear strain rate in the immediate vicinity of the bed. In Figure 13 (b), we use our model to match the height where rapid decrease of shear strain rate occurs in the borehole data ($A = 5.5$ m) and a typical Greenland atmospheric temperature ($T_s = -12°$C). Figure 13 (c) shows the vertical strain rate profile for a control run without basal topography. Only Figure 13 (b) is able to exhibit the observed drop in shear strain rate near the bed.

An important disconnect between Figures 13 (a) and (b-c) is the magnitude of the shear strain rate. Both of our model results show a shear strain rate that is about an order of magnitude higher than observed value in order to match the surface velocity of approximately 70 m/yr. Figures 13 (d-f) show the velocity profile with depth as inferred by Maier et al. (2019) from measurements (d), obtained from our simulations with basal topography (e), and without (f). Together, the panels demonstrate that our current model setup can either match the surface speed or the measured strain rates, but not both. The most likely explanation for this disconnect is that the observed surface speed is largely facilitated by basal sliding as sketched in Figure 13 (d), while the peak in shear strain rate may constitute the remnant of an internal shear band that may formed upstream when ice was still flowing over a topographicly variable bed.

In addition to borehole measurements of shear strain rate, our model could have important implication for depth-variability of ice fabric. For example, borehole data of grain size and cone angles collected at Siple Dome Antarctica by DiPrinzio et al. (2005) and reanalyzed by Pettit et al. (2011) reveals a localized band of small ice crystals and highly oriented fabric, located several hundred meters above the bed. Several processes could contribute to the development of this ice fabric with stress being a prominent factor, as supported by strain rate data. However, the observed shift in fabric occurs around the depth of the Holocene transition, highlighting that climate history may also play a role (Pettit et al., 2011). Despite its age, this ice fabric continues to control ice flow by partially decoupling of the flow field above and below the shear band. The flow field becomes three-dimensional, potentially to the degree of eddies forming (Meyer & Creyts, 2017).

We emphasize that our model only considers a simplified, hard-rock basal topography. In reality, subglacial beds are significantly more complex and dynamic. For example, a sharper topography is capable of generating more localization compared to a smooth sinusoidal shape. Nonetheless, the development of an internal shear band would still rely on similar physical processes, most importantly a positive accumulative energy gain.

The presence of tills or other sediments underneath the ice introduces further complexity, both from a dynamic and from a mechanical point of view (e.g., MacAyeal, 1989; King et al., 2009; Hoffman & Price, 2014; Minchew & Meyer, 2020) and a thermal point of view (e.g., Rempel, 2008; Christoffersen & Tulaczyk, 2003). One potentially interest-

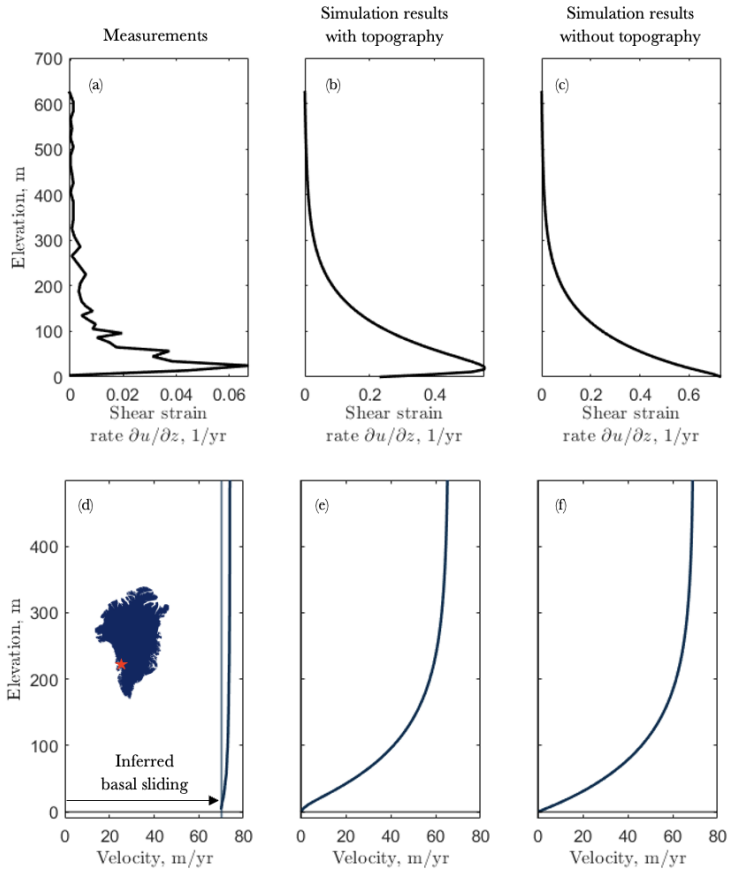

Figure 13. Comparison of model results to field measurements. The first column (a,d) shows the measurements at West Margin Greenland (Maier et al., 2019). Second (b,e) and third (c,f) columns show the simulation results with and without topography, respectively. The first row (a-c) shows the shear strain rates $\partial u/\partial z$ distribution in the depth direction. The second row (d-f) show the corresponding velocity profile for each case. In (d), the velocity profile is inferred by integrating the shear strain rate $\partial u/\partial z$ in (a) assuming there is basal sliding (Maier et al., 2019). Both simulations use the power-law rheology with exponent $n = 3$. The domain extend is set as 4800 m by 650 m. Bed height is set as 5.5 m and surface temperature is set as $-12°$C. In the second and third columns, the shear strain rates and velocity profiles are obtained at $x = 4235$ m.

ing implication of the flow separation we are identifying is that basal ice might interact in at least two distinct ways with a soft bad. One possibility is that fast ice motion and intense shear localization could lead to warm basal ice, generating interstitial water that drains to the bed. A thick layer of temperate can then form in topographical lows(Law et al., 2023) and create basal melt (Karlsson et al., 2021). Alternatively, basal ice in troughs may slow down because the shear band above it accommodates most of the deformation and cool down, potentially to the degree that underlying sediments freeze into the ice, as observed by Andreassen and Winsborrow (2009).

An important limitation of our study is the assumption of a two-dimensional model along the centerline (x, z) plane of an ice stream. This assumption neglects any variations in the transverse y direction, both in the ice flow and the shape of the basal topography. In reality, the transverse inflow could have a significant impact on temperature and hence shear band formation. Near the shear margin, for instance, the presence of

cold ice supplied from ice ridges leads to advective cooling, which counteracts viscous heating effects (Suckale et al., 2014; Meyer & Minchew, 2018; Hunter et al., 2021; Schoof & Mantelli, 2021). Basal topography is also three-dimensional, allowing the ice not only to move up and down of obstacles but also to flow around them. This lateral motion can mitigate some of the concentration of deformation that would occur exclusively at the peaks of the topography in the two-dimensional case we consider.

5 Conclusion

This study aims to investigate the influence of basal topography on the formation of internal shear band in ice flows using a thermo-mechanical Stokes flow model. By incorporating sinusoidal basal topography and comparing it with a flat topography control case, we observe extensive shear localization on topographic highs, resulting in the development of internal shear band. We analyze the impact of a power-law rheology with different exponents $n = 1, 2, 3, 4$ and find that non-linear rheology enhances shear heating, tilting the energy balance towards heating in the basal region of the ice. Moreover, we discover that the width of the internal shear band scales with the shape factor Ak raised to the power of $-2pn$, indicating that the development of the shear band is influenced by the topography shape. Specifically, higher values of Ak facilitate the connection and bridging of shear heating and shear deformation localization, increasing the likelihood of internal shear band formation. These findings contribute to the understanding of ice-sheet dynamics and provide insights for incorporating the spatial scale of the flow-to-sliding transition into ice-sheet models, such as Bueler (2009) .

6 Open Research

The current version of the numerical thermo-mechanical model with a build-in non-linear rheology model is available from DOI repository (Zenodo) at: `https://doi.org/10.5281/zenodo.7392224`. This model is developed based on the FastICE that can be found at: `https://doi.org/10.5281/zenodo.3461171` (Räss et al., 2020). The borehole data of shear deformation in Figure 13 (a) to compare against simulation results can be found from Maier et al. (2019). The basal topography data in Figure 12 (a) can be found at: `https://nsidc.org/data/idbmg4/versions/5` (Morlighem et al., 2017). The ice surface speed data in Figure 12 (b) can be found at: `10.5067/MEASURES/CRYOSPHERE/nsidc-0478.001` (Joughin et al., 2015). The basal topography data in Figure 12 (c) can be found at: `https://doi.pangaea.de/10.1594/PANGAEA.907918` (Franke et al., 2021).

Acknowledgments

This work was supported by the NSF CAREER grant # 2142651. We acknowledge helpful conversations about this work with Paul Summers, Daniel Martin, Dustin Schroeder, Eric Dunham, and Elisa Mantelli. We also appreciate the constructive inputs from Associate Editor Olga Sergienko and two anonymous reviewers.

References

Adalsteinsson, D., & Sethian, J. A. (1999). The fast construction of extension velocities in level set methods. *Journal of Computational Physics*, *148*(1), 2–22.

Adams, C. J., Iverson, N. R., Helanow, C., Zoet, L. K., & Bate, C. E. (2021). Softening of temperate ice by interstitial water. *Frontiers in Earth Science*, *9*, 702761.

Andreassen, K., & Winsborrow, M. (2009). Signature of ice streaming in bjørnøyrenna, polar north atlantic, through the pleistocene and implications for ice-stream dynamics. *Annals of Glaciology*, *50*(52), 17–26.

Bamber, J. L., Layberry, R. L., & Gogineni, S. (2001). A new ice thickness and bed data set for the greenland ice sheet: 1. measurement, data reduction, and errors. *Journal of Geophysical Research: Atmospheres*, *106*(D24), 33773–33780.

Barnes, P., Tabor, D., & Walker, J. (1971). The friction and creep of polycrystalline ice. *Proceedings of the Royal Society of London. A. Mathematical and Physical Sciences*, *324*(1557), 127–155.

Bindschadler, R. (2006). The environment and evolution of the west antarctic ice sheet: setting the stage. *Philosophical Transactions of the Royal Society A: Mathematical, Physical and Engineering Sciences*, *364*(1844), 1583–1605.

Bingham, R. G., & Siegert, M. J. (2007). Radar-derived bed roughness characterization of institute and möller ice streams, west antarctica, and comparison with siple coast ice streams. *Geophysical Research Letters*, *34*(21).

Bueler, J., Ed Brown. (2009). Shallow shelf approximation as a "sliding law" in a thermomechanically coupled ice sheet model. *Journal of Geophysical Research: Earth Surface*, *114*(F3).

Carsey, F., Behar, A., Lane, A. L., Realmuto, V., & Engelhardt, H. (2002). A borehole camera system for imaging the deep interior of ice sheets. *Journal of Glaciology*, *48*(163), 622–628.

Christoffersen, P., & Tulaczyk, S. (2003). Thermodynamics of basal freeze-on: predicting basal and subglacial signatures of stopped ice streams and interstream ridges. *Annals of Glaciology*, *36*, 233–243.

Clarke, G. K. (1987). Fast glacier flow: Ice streams, surging, and tidewater glaciers. *Journal of Geophysical Research: Solid Earth*, *92*(B9), 8835–8841.

Clarke, G. K., Nitsan, U., & Paterson, W. (1977). Strain heating and creep instability in glaciers and ice sheets. *Reviews of Geophysics*, *15*(2), 235–247.

DiPrinzio, C., Wilen, L. A., Alley, R., Fitzpatrick, J., Spencer, M., & Gow, A. (2005). Fabric and texture at siple dome, antarctica. *Journal of Glaciology*, *51*(173), 281–290.

Doyle, S. H., Hubbard, B., Christoffersen, P., Young, T. J., Hofstede, C., Bougamont, M., et al. (2018). Physical conditions of fast glacier flow: 1. measurements from boreholes drilled to the bed of store glacier, west greenland. *Journal of Geophysical Research: Earth Surface*, *123*(2), 324–348.

Echelmeyer, K., & Zhongxiang, W. (1987). Direct observation of basal sliding and deformation of basal drift at sub-freezing temperatures. *Journal of Glaciology*, *33*(113), 83–98.

Fowler. (2001). Modelling the flow of glaciers and ice sheets. In *Continuum mechanics and applications in geophysics and the environment* (pp. 201–221). Springer.

Fowler. (2010). Weertman, lliboutry and the development of sliding theory. *Journal of Glaciology*, *56*(200), 965–972.

Franke, S., Jansen, D., Beyer, S., Neckel, N., Binder, T., Paden, J., & Eisen, O. (2021). Complex basal conditions and their influence on ice flow at the onset of the northeast greenland ice stream. *Journal of Geophysical Research: Earth Surface*, *126*(3), e2020JF005689.

Glen. (1952). Experiments on the deformation of ice. *Journal of Glaciology*, *2*(12), 111–114.

Glen. (1955). The creep of polycrystalline ice. *Proceedings of the Royal Society of London. Series A. Mathematical and Physical Sciences*, *228*(1175), 519–538.

Goldsby, D., & Kohlstedt, D. L. (2001). Superplastic deformation of ice: Experimental observations. *Journal of Geophysical Research: Solid Earth*, *106*(B6), 11017–11030.

Goodwin, I. D. (1993). Basal ice accretion and debris entrainment within the coastal ice margin, law dome, antarctica. *Journal of Glaciology*, *39*(131), 157–166.

Gow, A., Epstein, S., & Sheehy, W. (1979). On the origin of stratified debris in ice cores from the bottom of the antarctic ice sheet. *Journal of Glaciology*, *23*(89), 185–192.

Gudmundsson, G. H. (1997). Basal-flow characteristics of a non-linear flow sliding frictionless over strongly undulating bedrock. *Journal of Glaciology*, *43*(143), 80–89.

Harrington, J. A., Humphrey, N. F., & Harper, J. T. (2015). Temperature distribution and thermal anomalies along a flowline of the greenland ice sheet. *Annals of Glaciology*, *56*(70), 98–104.

Helanow, C., Iverson, N. R., Woodard, J. B., & Zoet, L. K. (2021). A slip law for hard-bedded glaciers derived from observed bed topography. *Science Advances*, *7*(20), eabe7798.

Helanow, C., Iverson, N. R., Zoet, L. K., & Gagliardini, O. (2020). Sliding relations for glacier slip with cavities over three-dimensional beds. *Geophysical Research Letters*, *47*(3), e2019GL084924.

Hermann, E., & Barclay, K. (1998). Basal sliding of ice stream b, west antarctica. *Journal of Glaciology*, *44*(147), 223–230.

Herron, S., Langway, C. C., et al. (1979). The debris-laden ice at the bottom of the greenland ice sheet. *Journal of Glaciology*, *23*(89), 193–207.

Hills, B. H., Harper, J. T., Humphrey, N. F., & Meierbachtol, T. W. (2017). Measured horizontal temperature gradients constrain heat transfer mechanisms in greenland ice. *Geophysical Research Letters*, *44*(19), 9778–9785.

Hoffman, M., & Price, S. (2014). Feedbacks between coupled subglacial hydrology and glacier dynamics. *Journal of Geophysical Research: Earth Surface*, *119*(3), 414–436.

Hunter, P., Meyer, C., Minchew, B., Haseloff, M., & Rempel, A. (2021). Thermal controls on ice stream shear margins. *Journal of Glaciology*, *67*(263), 435–449.

Joughin, I., Rignot, E., Rosanova, C. E., Lucchitta, B. K., & Bohlander, J. (2003). Timing of recent accelerations of pine island glacier, antarctica. *Geophysical Research Letters*, *30*(13).

Joughin, I., Smith, B., Howat, I., & Scambos, T. (2015). *Measures greenland ice sheet velocity map from insar data, version 2.* NASA National Snow and Ice Data Center Distributed Active Archive Center. Retrieved from `https://nsidc.org/data/NSIDC-0478/versions/2` doi: 10.5067/OC7B04ZM9G6Q

Joughin, I., Smith, B. E., Howat, I. M., Scambos, T., & Moon, T. (2010). Greenland flow variability from ice-sheet-wide velocity mapping. *Journal of Glaciology*, *56*(197), 415–430.

Karlsson, N. B., Solgaard, A. M., Mankoff, K. D., Gillet-Chaulet, F., MacGregor, J. A., Box, J. E., et al. (2021). A first constraint on basal melt-water production of the greenland ice sheet. *Nature Communications*, *12*(1), 3461.

King, E. C., Hindmarsh, R. C., & Stokes, C. (2009). Formation of mega-scale glacial lineations observed beneath a west antarctic ice stream. *Nature Geoscience*, *2*(8), 585–588.

Krabbendam, M. (2016). Sliding of temperate basal ice on a rough, hard bed: creep mechanisms, pressure melting, and implications for ice streaming. *The Cryosphere*, *10*(5), 1915–1932.

Kreiss, H.-O. (1968). Stability theory for difference approximations of mixed initial boundary value problems. i. *Mathematics of Computation*, *22*(104), 703–714.

Larson, F. . (1980). The uniqueness of steady state flows of glaciers and ice sheets. *Geophysical Journal International*, *63*(2), 333–345.

Law, R., Christoffersen, P., MacKie, E., Cook, S., Haseloff, M., & Gagliardini, O. (2023). Complex motion of greenland ice sheet outlet glaciers with basal temperate ice. *Science Advances*, *9*(6), eabq5180.

Lliboutry, L. (1968). General theory of subglacial cavitation and sliding of temperate glaciers. *Journal of Glaciology*, *7*(49), 21–58.

Lüthi, M., Funk, M., Iken, A., Gogineni, S., & Truffer, M. (2002). Mechanisms of fast flow in jakobshavn isbræ, west greenland: Part iii. measurements of ice deformation, temperature and cross-borehole conductivity in boreholes to the bedrock. *Journal of Glaciology*, *48*(162), 369–385.

MacAyeal, D. R. (1989). Large-scale ice flow over a viscous basal sediment: Theory and application to ice stream b, antarctica. *Journal of Geophysical Research: Solid Earth*, *94*(B4), 4071–4087.

Maier, N., Humphrey, N., Harper, J., & Meierbachtol, T. (2019). Sliding dominates slow-flowing margin regions, greenland ice sheet. *Science Advances*, *5*(7), eaaw5406.

Mantelli, E., Haseloff, M., & Schoof, C. (2019). Ice sheet flow with thermally activated sliding. part 1: the role of advection. *Proceedings of the Royal Society A*, *475*(2230), 20190410.

Maule, C. F., Purucker, M. E., Olsen, N., & Mosegaard, K. (2005). Heat flux anomalies in antarctica revealed by satellite magnetic data. *Science*, *309*(5733), 464–467.

Mellor, M., & Testa, R. (1969). Effect of temperature on the creep of ice. *Journal of Glaciology*, *8*(52), 131–145.

Meyer, C. R., & Creyts, T. T. (2017). Formation of ice eddies in subglacial mountain valleys. *Journal of Geophysical Research: Earth Surface*, *122*(9), 1574–1588.

Meyer, C. R., & Minchew, B. M. (2018). Temperate ice in the shear margins of the antarctic ice sheet: Controlling processes and preliminary locations. *Earth and Planetary Science Letters*, *498*, 17–26.

Minchew, B. M., & Meyer, C. R. (2020). Dilation of subglacial sediment governs incipient surge motion in glaciers with deformable beds. *Proceedings of the Royal Society A*, *476*(2238), 20200033.

Morlighem, M., Williams, C. N., Rignot, E., An, L., Arndt, J. E., Bamber, J. L., et al. (2017). Bedmachine v3: Complete bed topography and ocean bathymetry mapping of greenland from multibeam echo sounding combined with mass conservation. *Geophysical Research Letters*, *44*(21), 11–051.

Mouginot, J., Rignot, E., & Scheuchl, B. (2014). Sustained increase in ice discharge from the amundsen sea embayment, west antarctica, from 1973 to 2013. *Geophysical Research Letters*, *41*(5), 1576–1584.

Nye. (1959). The motion of ice sheets and glaciers. *Journal of Glaciology*, *3*(26), 493–507.

Nye. (1969). A calculation on the sliding of ice over a wavy surface using a newtonian viscous approximation. *Proceedings of the Royal Society of London. A. Mathematical and Physical Sciences*, *311*(1506), 445–467.

Nye. (1971). Causes and mechanics of glacier surges: discussion. *Canadian Journal of Earth Sciences*, *8*(2), 306–307.

Orlanski, I. (1976). A simple boundary condition for unbounded hyperbolic flows. *Journal of Computational Physics*, *21*(3), 251–269.

Osher, S., Fedkiw, R., & Piechor, K. (2004). Level set methods and dynamic implicit surfaces. *Applied Mechanics Reviews*, *57*(3), B15–B15.

Osher, S., & Sethian, J. A. (1988). Fronts propagating with curvature-dependent

speed: Algorithms based on hamilton-jacobi formulations. *Journal of Computational Physics*, *79*(1), 12–49.

Paterson, W. S. B. (1994). *Physics of glaciers*. Butterworth-Heinemann.

Peskin. (1972). *Flow patterns around heart valves: a digital computer method for solving the equations of motion*. Yeshiva University.

Peskin. (2002). The immersed boundary method. *Acta Numerica*, *11*, 479-517. Retrieved from https://doi.org/10.1080/00207540701450013 doi: doi:10.1017/S0962492902000077

Petrat, N., Zhu, H., Stadler, G., Hughes, T. J., & Ghattas, O. (2012). An inexact gauss-newton method for inversion of basal sliding and rheology parameters in a nonlinear stokes ice sheet model. *Journal of Glaciology*, *58*(211), 889–903.

Pettit, E. C., Waddington, E. D., Harrison, W. D., Thorsteinsson, T., Elsberg, D., Morack, J., & Zumberge, M. A. (2011). The crossover stress, anisotropy and the ice flow law at siple dome, west antarctica. *Journal of Glaciology*, *57*(201), 39–52.

Qin, Z., Delaney, K., Riaz, A., & Balaras, E. (2015). Topology preserving advection of implicit interfaces on cartesian grids. *Journal of Computational Physics*, *290*, 219–238.

Räss, L., Licul, A., Herman, F., Podladchikov, Y. Y., & Suckale, J. (2020). Modelling thermomechanical ice deformation using an implicit pseudo-transient method (fastice v1. 0) based on graphical processing units (gpus). *Geoscientific Model Development*, *13*(3), 955–976.

Rempel, A. (2008). A theory for ice-till interactions and sediment entrainment beneath glaciers. *Journal of Geophysical Research: Earth Surface*, *113*(F1).

Rignot, E., & Mouginot, J. (2012). Ice flow in greenland for the international polar year 2008–2009. *Geophysical Research Letters*, *39*(11).

Rignot, E., Mouginot, J., & Scheuchl, B. (2011). Ice flow of the antarctic ice sheet. *Science*, *333*(6048), 1427–1430.

Rignot, E., Vaughan, D. G., Schmeltz, M., Dupont, T., & MacAyeal, D. (2002). Acceleration of pine island and thwaites glaciers, west antarctica. *Annals of Glaciology*, *34*, 189–194.

Robin. (1955). Ice movement and temperature distribution in glaciers and ice sheets. *Journal of Glaciology*, *2*(18), 523–532.

Ryser, C., Lüthi, M. P., Andrews, L. C., Hoffman, M. J., Catania, G. A., Hawley, R. L., et al. (2014). Sustained high basal motion of the greenland ice sheet revealed by borehole deformation. *Journal of Glaciology*, *60*(222), 647–660.

Räss, L., Utkin, I., Duretz, T., Omlin, S., & Podladchikov, Y. Y. (2022, July). Assessing the robustness and scalability of the accelerated pseudo-transient method. *Geoscientific Model Development*, *15*(14), 5757–5786. Retrieved 2022-10-19, from https://gmd.copernicus.org/articles/15/5757/2022/ doi: 10.5194/gmd-15-5757-2022

Schmid, D. W., & Podladchikov, Y. Y. (2003). Analytical solutions for deformable elliptical inclusions in general shear. *Geophysical Journal International*, *155*(1), 269–288.

Schoof, C. (2005). The effect of cavitation on glacier sliding. *Proceedings of the Royal Society A: Mathematical, Physical and Engineering Sciences*, *461*(2055), 609–627.

Schoof, C., & Mantelli, E. (2021). The role of sliding in ice stream formation. *Proceedings of the Royal Society A*, *477*(2248), 20200870.

Sethian, J. A. (1999). *Level set methods and fast marching methods: evolving interfaces in computational geometry, fluid mechanics, computer vision, and materials science* (Vol. 3). Cambridge university press.

Sethian, J. A., & Smereka, P. (2003). Level set methods for fluid interfaces. *Annual Review of Fluid Mechanics*, *35*(1), 341–372.

Shapiro, N. M., & Ritzwoller, M. H. (2004). Inferring surface heat flux distributions

guided by a global seismic model: particular application to antarctica. *Earth and Planetary Science Letters*, *223*(1-2), 213–224.

Siegert, M. J., Taylor, J., Payne, A. J., & Hubbard, B. (2004). Macro-scale bed roughness of the siple coast ice streams in west antarctica. *Earth Surface Processes and Landforms: The Journal of the British Geomorphological Research Group*, *29*(13), 1591–1596.

Suckale, J., Platt, J. D., Perol, T., & Rice, J. R. (2014). Deformation-induced melting in the margins of the west antarctic ice streams. *Journal of Geophysical Research: Earth Surface*, *119*(5), 1004–1025.

Uhlmann, M. (2005). An immersed boundary method with direct forcing for the simulation of particulate flows. *Journal of Computational Physics*, *209*(2), 448–476.

Weertman, J. (1957). On the sliding of glaciers. *Journal of Glaciology*, *3*(21), 33–38.

Whillans, I., Bolzan, J., & Shabtaie, S. (1987). Velocity of ice streams b and c, antarctica. *Journal of Geophysical Research: Solid Earth*, *92*(B9), 8895–8902.

Wright, A., Young, D., Roberts, J., Schroeder, D., Bamber, J., Dowdeswell, J., ... others (2012). Evidence of a hydrological connection between the ice divide and ice sheet margin in the aurora subglacial basin, east antarctica. *Journal of Geophysical Research: Earth Surface*, *117*(F1).

Yuen, D. A., & Schubert, G. (1979). The role of shear heating in the dynamics of large ice masses. *Journal of Glaciology*, *24*(90), 195–212.

Appendix A Scaling of energy equation

To identify the relative magnitude of the terms in energy equation (9), we carry out a scaling analysis. We choose the characteristic parameters to be

$$\bar{z} = H,\ \bar{\tau} = \rho_{\mathrm{i}} g L_z \alpha,\ \bar{u} = U_s,\ \bar{T} = T_0,\ \bar{\dot{\epsilon}} = \frac{U_s}{H}, \tag{A1}$$

where $H = 1000$ m is the characteristic ice thickness, $U_s = 100$ m/yr is the characteristic surface speed, $T_0 = -26°\mathrm{C}$ is a typical atmospheric temperature in Antarctica, $\alpha = 2°$ is the characteristic bed slope. Other relevant constants are: specific heat of ice $c_p = 2096.9\ \mathrm{J/(kg \cdot K)}$, ice density $\rho_{\mathrm{i}} = 900\ \mathrm{kg/m^3}$, thermal conductivity $\kappa = 2.51\mathrm{W/(m \cdot K)}$. As a characteristic vertical speed (or thinning speed), we assume the $U_t \sim U_s \times 10^{-2}$. Substitute in the characteristic values and the constants, we have the scalings of the spatial terms

$$\rho c_p \left(u_i \frac{\partial T}{\partial x_i} \right) \sim \mathcal{O}(10^{-3}),\ \frac{\partial}{\partial x_i} \left(\kappa \frac{\partial T}{\partial x_i} \right) \sim \mathcal{O}(10^{-5}),\ \tau_E \dot{\epsilon}_E \sim \mathcal{O}(10^{-3}). \tag{A2}$$

Note that in our problem setting of a slab of ice flowing down a slope, the dominant shear strain rate is the shear strain rate $\dot{\epsilon}_{xz}$ and the dominant advection is the vertical advection $U_t(\partial T/\partial z)$.

Appendix B Scaling of momentum equation

Assume a generic power-law rheology without temperature dependence, and also assume that the dominant strain rate in the basal region is the shear strain rate. The viscosity can be then expressed as

$$\eta = \frac{1}{2} a_0^{-\frac{1}{n}} \left(\frac{\partial u}{\partial z} \right)^{-1+\frac{1}{n}}. \tag{B1}$$

Substitute in the viscosity, the x momentum equation 35 is

$$\eta\frac{\partial^2 u}{\partial x^2}+\frac{1}{n}\eta\frac{\partial^2 u}{\partial z^2}=\rho g\alpha, \tag{B2}$$

$$\frac{\partial^2 u}{\partial x^2}+\frac{1}{n}\frac{\partial^2 u}{\partial z^2}=2a_0^{\frac{1}{n}}\left(\frac{\partial u}{\partial z}\right)^{1-\frac{1}{n}}\rho g\alpha. \tag{B3}$$

Assume the characteristic horizontal length l. For the sinusoidal topography, we consider l to be $\sim \lambda^{(n-1)p}kA^{1-(n-1)p}$, where p is some constant and n is the power-low exponent. We choose $(n-1)$ to avoid zero denominator in the later derivation. Finally the x momentum equation can be expressed as

$$\left(\frac{1}{l^2}+\frac{1}{n}\frac{1}{B_w^2}\right)=C\frac{1}{B_w^{1-\frac{1}{n}}}, \tag{B4}$$

where $C=2\rho g\alpha a_0^{\frac{1}{n}}u^{-\frac{1}{n}}$. Simplify the equation, we have the following relationship

$$B_w^2-Cl^2B_w^{\frac{1}{n}+1}+\frac{l^2}{n}=0 \tag{B5}$$

$$l^2=\frac{nB_w^2}{CnB_w^{\frac{1}{n}+1}-1} \tag{B6}$$

Substitute representative numbers of $\rho = 900$ kg/m^3, $g = 9.8$ m/s^2, $a_0 \sim 10^{-10}-10^{-13}$, $u\sim 100$ m/yr, $B_w\sim 50-500$ m, we have $CnB_w^{\frac{1}{n}+1}\sim 10^2-10^3$, thus the relationship between l and B_w can be further simplified to

$$l^2=\frac{nB_w^2}{CnB_w^{\frac{1}{n}+1}} \tag{B7}$$

$$B_w\propto l^{\frac{2n}{n-1}} \tag{B8}$$

We further substitute $Ak = 2\pi A/\lambda$, the above relationship can be alternatively expressed as

$$B_w\propto (Ak)^{-2pn} \tag{B9}$$

Appendix C Velocity ratio distribution for different n and topographies

.

.

Figures C1 and C2 depict contour lines ranging from 15% to 95% of the surface speed U_s, with each contour line spaced by 5% of U_s. When Ak is low, the velocity ratio contours exhibit higher concentration around the peak region and a relatively more evenly spaced distribution around the trough. This behavior indicates that the ice experiences vertical compression and extension as it flows over basal topography. Furthermore, this observation suggests that the perturbations originating from the basal topography propagate upwards from the bed to the surface over distances spanning tens to several hundred meters. In contrast, when Ak is high, the velocity ratio contours tend to concentrate at a consistent elevation and do not align with the shape of the basal topography. Thus ice no longer experiences the alternation between vertical compression and extension as flows downstream. This outcome implies that the actual form of the basal topography exerts significantly less influence on the internal ice, and the flow becomes detached to a considerable extent from the true shape of the basal topography.

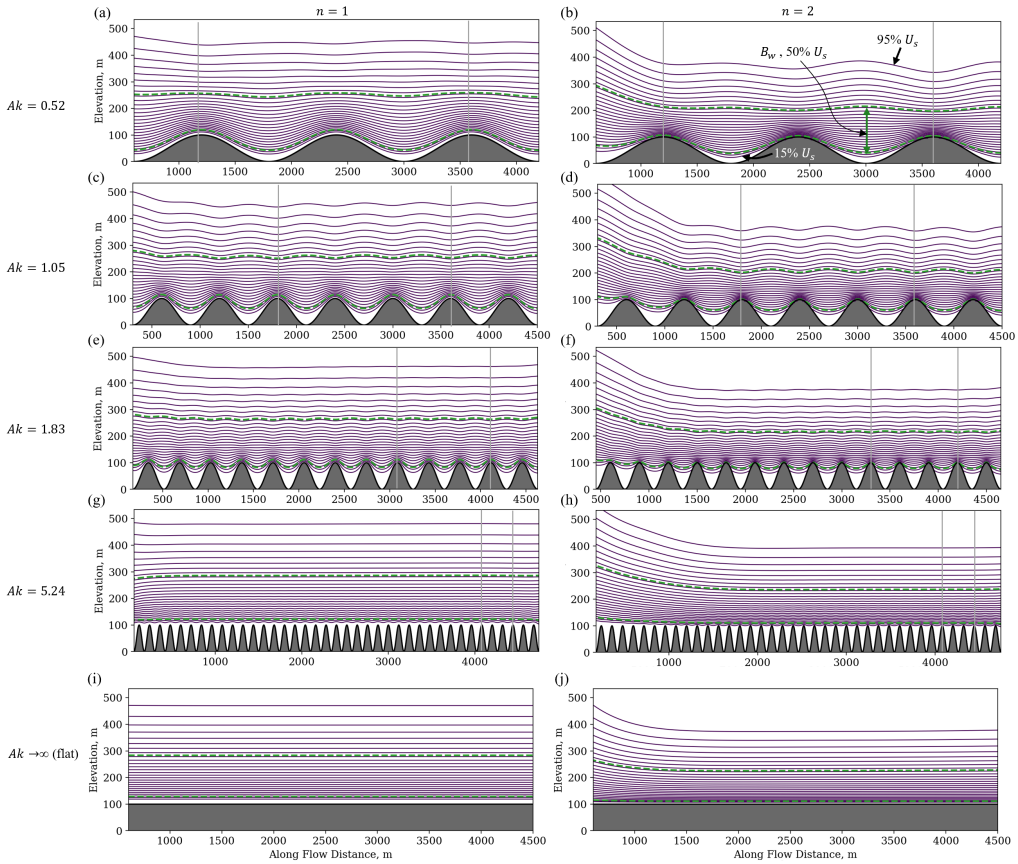

Figure C1. The velocity ratio (local x velocity divided by the surface x velocity in the same ice column) contours for $n = 1, 2$ and differnet Ak. Each row corresponds to a different shape factor: $Ak = 0.52, 1.05, 1.83, 5.24$, and ∞ (representing a flat bed). The first and second column represente the case where $n = 1$ and $n = 2$, respectively. In each panel, the purple lines show the contour lines from $95\%U_s$ to $15\%U_s$, with a separation of $3\%U_s$. The two green dashed lines represent the contour lines of 70% U_s and 20% U_s, which define the internal shear band upper and lower bounds. Grey vertical lines indicate the spatial x locations where we calculate the average internal shear bandwidth.

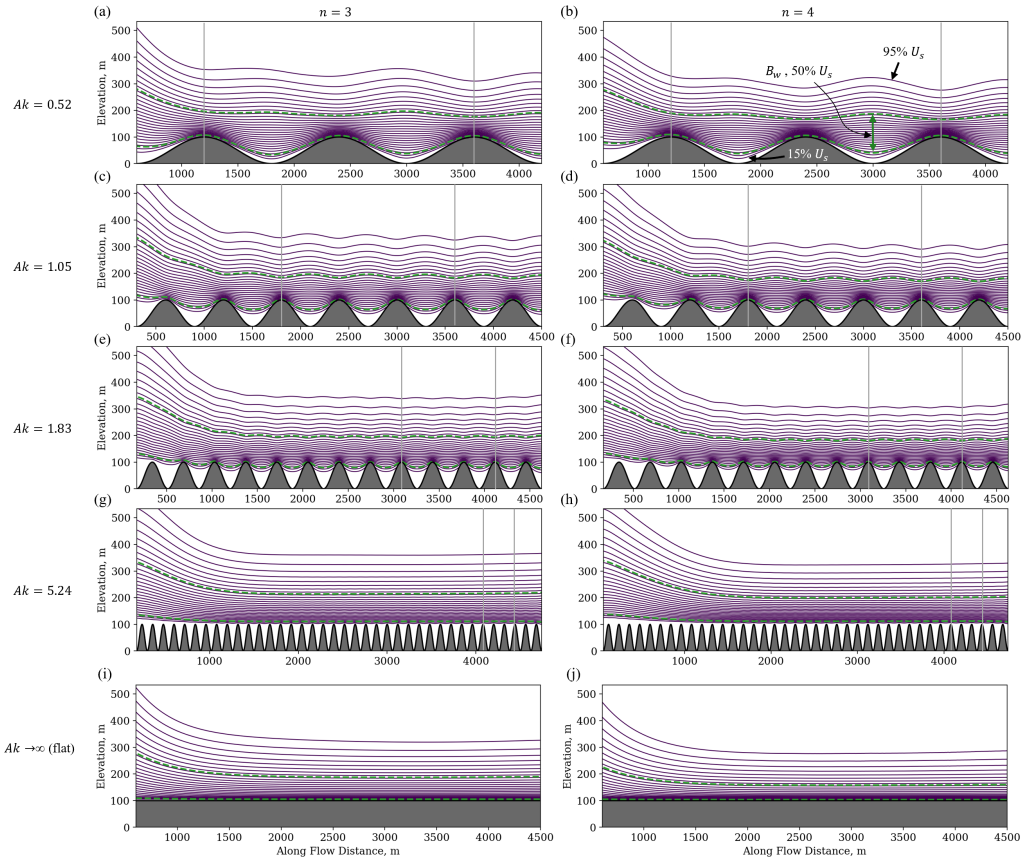

Figure C2. The velocity ratio contours for different $n = 3, 4$ and different Ak. The layout of this figure follows the same as Figure C1